

Cyclic complex spin state evolution of defunct GEO satellites

Conor J. Benson and Daniel J. Scheeres

*University of Colorado Boulder
429 UCB, Boulder, CO 80309*

William H. Ryan and Eileen V. Ryan

*Magdalena Ridge Observatory, New Mexico Institute of Mining and Technology
101 East Road, Socorro, NM 87801*

ABSTRACT

The significant spin state changes of some defunct GEO satellites have been attributed to solar radiation torques through the Yarkovsky-O'Keefe-Radzievskii-Paddack (YORP) effect. It is hypothesized that some satellites cycle between complex and uniform rotation due to the combined influences of YORP and internal energy dissipation. To explore this hypothesis, aperiodic light curves of the defunct GOES 8 weather satellite spanning several years were analyzed. Leveraging torque-free rigid body dynamics assumptions as well as the satellite's known mass properties, geometry, and surface materials, simulated light curve surveys were conducted with a high fidelity model to better understand how the fundamental tumbling periods manifest themselves in observations. Using strong trends resulting from the surveys, well-fitting rotation states were obtained at each observation epoch. These rotation states indicate that after the rapid, well-documented spin down in early-mid 2014, the satellite went through at least one complete spin cycle between late 2014 and early 2018, with its effective spin period varying between 5 and least 40 minutes over this span. The aperiodic nature of the observations indicates that the satellite remained in at least mildly complex rotation over this roughly three year period.

1. INTRODUCTION

With the growing value of GEO for communications and observation, understanding and predicting the motion of GEO debris becomes increasingly important. Defunct satellites constitute a large fraction of the GEO debris population. The orbital evolution of these satellites has been studied extensively, but little is known about their rotational dynamics. However, many defunct GEO satellites have evolving spin states [1,2,3]. Albuja et al. show that the observed spin period evolution of the defunct GOES 8 and 10 weather satellites (NORAD 23051 and 24786) can be explained by solar radiation torques generated through the Yarkovsky-O'Keefe-Radzievskii-Paddack (YORP) effect [4,5]. YORP torques have been observed to alter the spin states of small asteroids [6]. Albuja et al. also hypothesize that YORP and kinetic energy dissipation from structural flexibility and residual fuel slosh may cause some satellites to cycle between uniform and complex rotation (i.e. non-principal axis tumbling). As a satellite's uniform spin rate decreases due to YORP, it loses spin stability. At some small non-zero spin rate, YORP then preferentially spins up the long axis, the most easily accelerated by external torques. Such behavior was observed by Albuja et al. in GOES 8 dynamical simulations. During tumbling spin up, they predict that energy dissipation will eventually overpower YORP, driving the satellite back towards uniform rotation, the lowest energy state for a given angular momentum. Better knowledge of defunct satellite spin state evolution stands to improve attitude dependent SRP modeling for long-term orbit prediction and aid on-orbit debris mitigation and satellite servicing efforts where rotation state information is crucial for grappling and docking operations.

In this paper, we further explore the cyclic spin state evolution hypothesis by extracting plausible rotation states from an ensemble of GOES 8 light curves taken over several years. First, the GOES satellites and observations of interest will be presented. We will then discuss tumbling dynamics relevant to light curve inversion. This will be followed by discussion of the high fidelity light curve simulator and surveys used to better understand observed light curve frequencies and test candidate rotation states. The best-fitting rotation states for each light curve will then be presented along with a discussion of the satellite's overall dynamical evolution.

2. GOES SATELLITES

The five defunct GOES 8-12 weather satellites are ideal for testing this cyclic evolution hypothesis. Built to nearly identical specification by Space Systems/Loral and sequentially retired between 2004 and 2013, their significant asymmetry and long appendages make these satellites highly susceptible to YORP torques and energy dissipation. A model of the GOES 8 satellite is included in Fig. 1. Each satellite features a single 4.8 m long solar array opposed by a 3.3 m conical solar sail mounted on a 17.7 m deployable boom [7]. The solar sail's purpose is to counter the solar radiation torque generated by the solar array. To finely balance the net torque, an adjustable, highly reflective trim tab is mounted on the end of the solar array. This configuration effectively balances the solar torque during normal sun-pointing operations, but significant net torques can be generated in uncontrolled scenarios. Another advantage of studying the GOES satellites is that their end of life mass properties, solar array and trim tab geometry, and surface materials are well documented, greatly assisting light curve inversion and dynamical modeling.

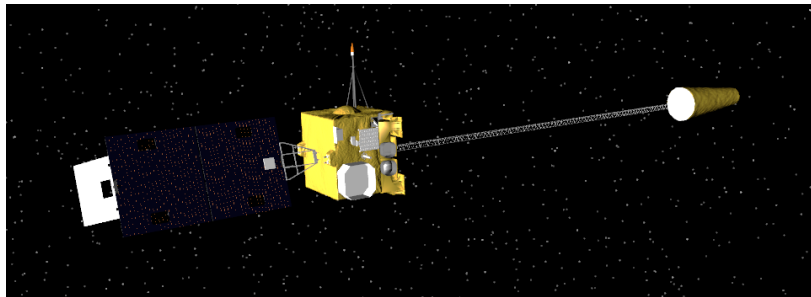
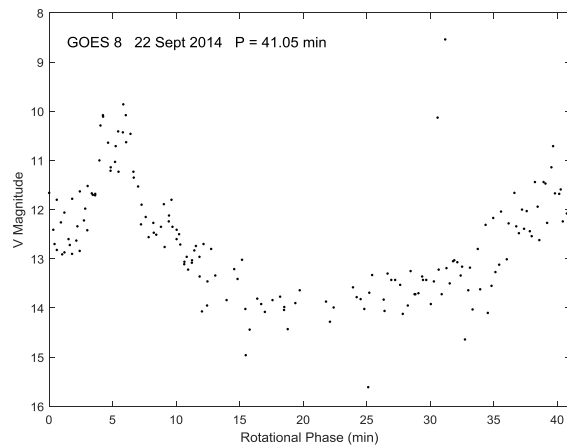
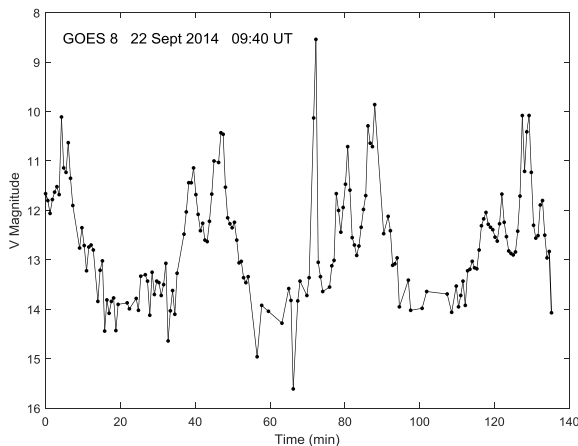


Fig. 1. Model of GOES 8 satellite in estimated end of life configuration

3. OBSERVATIONS

Given these ideal characteristics, the GOES 8-12 satellites have been observed periodically at the Maui Research and Technology Center, Naval Observatory Flagstaff Station (NOFS), as well as Magdalena Ridge and Lowell Observatories since 2013. GOES 8 is particularly intriguing, with its uniform spin period steadily increasing from 16.48 s to 75.66 s between February and July 2014 [2,3]. YORP dynamics simulations conducted by Albuja et al. suggested the satellite would continue decelerating, enter a tumbling state, and spin up about its long axis. Both the observed evolution and simulations suggested a zero spin rate intercept in late August or early September 2014. In September 2014, the USNO COTS instrument obtained the following observations in Fig. 2. These data were collected at a 37 s sampling cadence with 32 s exposures and have been calibrated to apparent V magnitude. Both light curves in Fig. 2 fold well on periods of ~ 40 min, suggesting that the satellite is in fact rotating slowly and that a much faster spin period is not being under sampled. The variations in light curve structure over successive rotations may be due to mildly complex rotation or changing phase angle. So no definitive conclusions can be drawn about uniform or complex rotation. Also, the light curves fold best over successively shorter periods, suggesting possible spin up. Nevertheless, the 1.25 min difference may due to varying synodic (observed) periods.



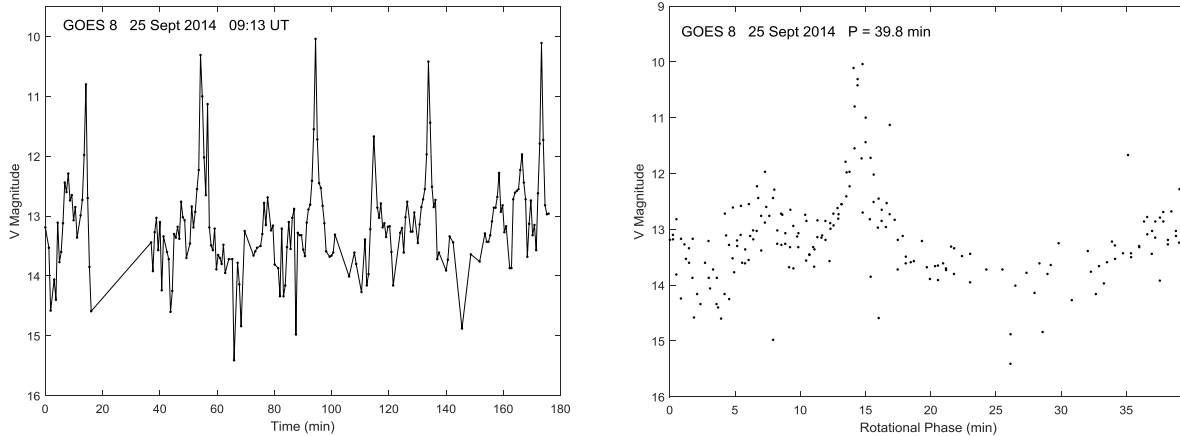


Fig. 2. Sequential and phase folded September 2014 GOES 8 light curves (USNO COTS)

Figures 3 and 4 show light curves obtained by Ryan & Ryan with the Magdalena Ridge Observatory (MRO) 2.4 m telescope on 12 and 28 September 2015 [3]. All MRO observations were taken using an Andor iKon 936 CCD camera and Bessel VR or R filter. Images were taken at a rate of ~ 1 Hz with ~ 0.6 s exposures and reduced using the IRAF *phot* task, yielding instrumental magnitudes. These observations suggest significantly faster rotation than a year before. The 12 September observations are not clearly periodic, while those on 28 September fold on a period of 14.46 ± 0.05 min. Nevertheless, the amplitudes of later peaks are more variable, suggesting complex rotation.

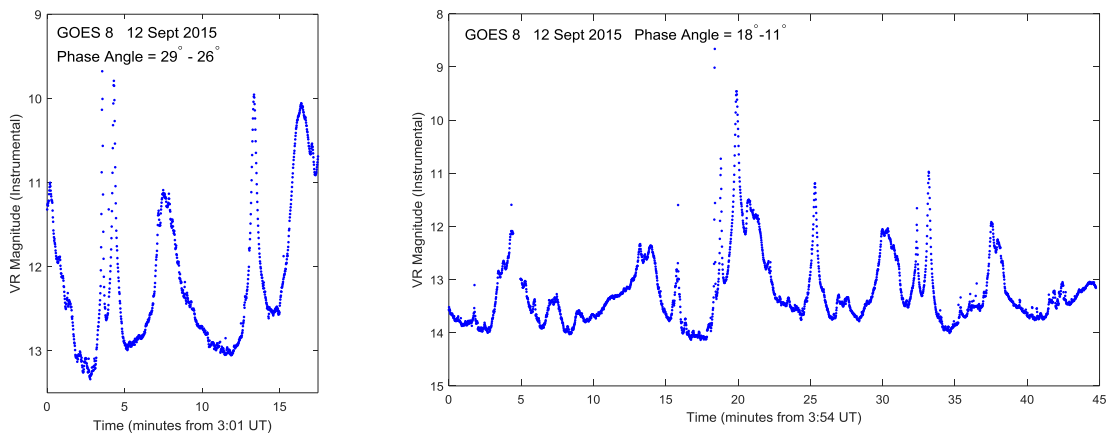


Fig. 3. 12 September 2015 GOES 8 light curves (MRO 2.4 m)

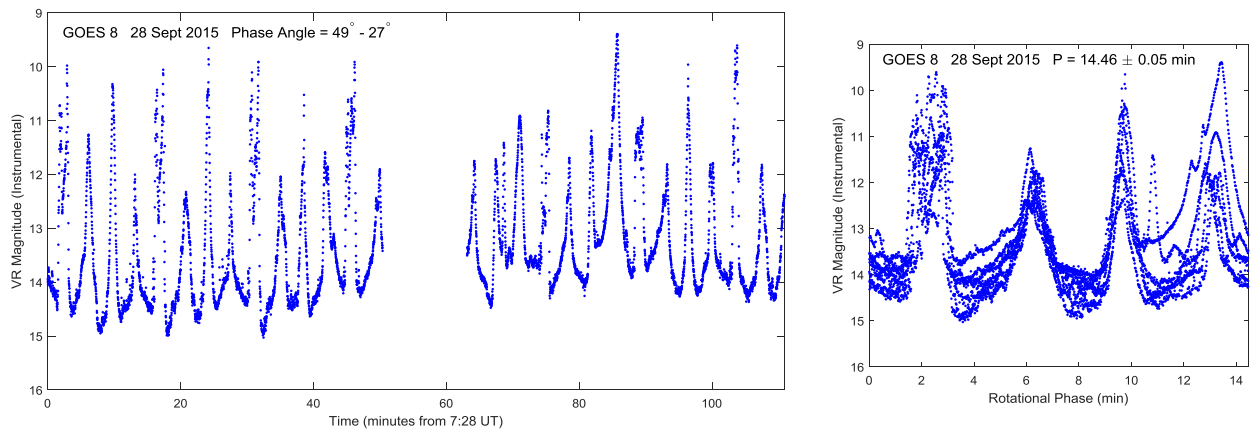


Fig. 4. Sequential and phase folded 28 September 2015 GOES 8 light curves (MRO 2.4 m)

Observations obtained on 6 February 2016 with the MRO 2.4 m telescope are provided in Fig. 5. The best fit phase folded period for these observations is 13.63 ± 0.1 min although there is significant dispersion in the first and third peaks as seen in Fig. 5. This again suggests that the satellite is actually tumbling although these differences could be due to changing phase angle.

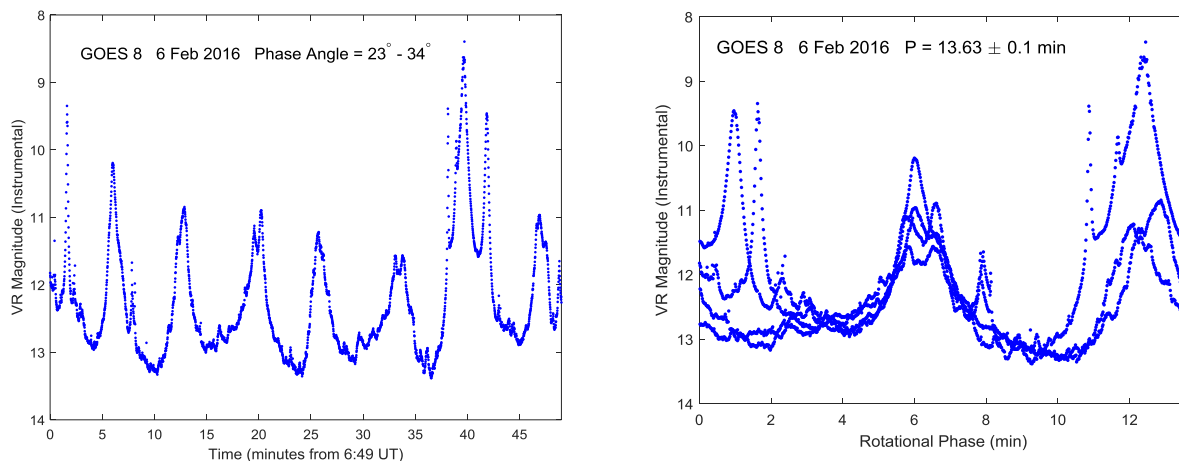


Fig. 5. Sequential and phase folded 6 February 2016 GOES 8 light curves (MRO 2.4 m)

The 3 Jul 2016 observations shown in Fig. 6 were collected using Lowell Observatory’s 1.1 m Hall telescope fitted with an EV2 CCD231 CCD camera and VR filter. Images were taken with 1 s exposures at a cadence of 11 s, the majority of which was required for CCD readout. Images were reduced using IRAF and a custom IDL pipeline. The magnitudes were then calibrated against the 2MASS star catalogue. Data contaminated by field stars were removed. Repointing was required due to the use of constant rate tracking, resulting in a ~5 min observation gap. In spite of this gap and the relatively low sampling rate, the light curve does not exhibit defined periodicity. The 14 July 2016 observations (plotted in Fig. 6) were collected using Lowell’s 1.8 m Perkins telescope fitted with the PRISM 2048×2064 pixel CCD camera and R filter. As before, images were taken with 1 s exposures but at a faster cadence of 7 s. The reduction process was the same as for the 3 Jul 2016 observations except that only instrumental magnitudes were obtained. As with the light curve from two weeks prior, there is no defined periodicity. An interesting feature in the 14 Jul 2016 light curve is the rapid drop in mean magnitude over time. The small change in solar phase angle (only 4°), suggests this may be due to complex rotation rather than varying lighting geometry. Compared to the 6 Feb 2016 data, those from July 2016 have higher frequencies, suggesting a spin rate increase over this timespan. Nevertheless, these changes in observed frequencies may be due to different viewing geometry.

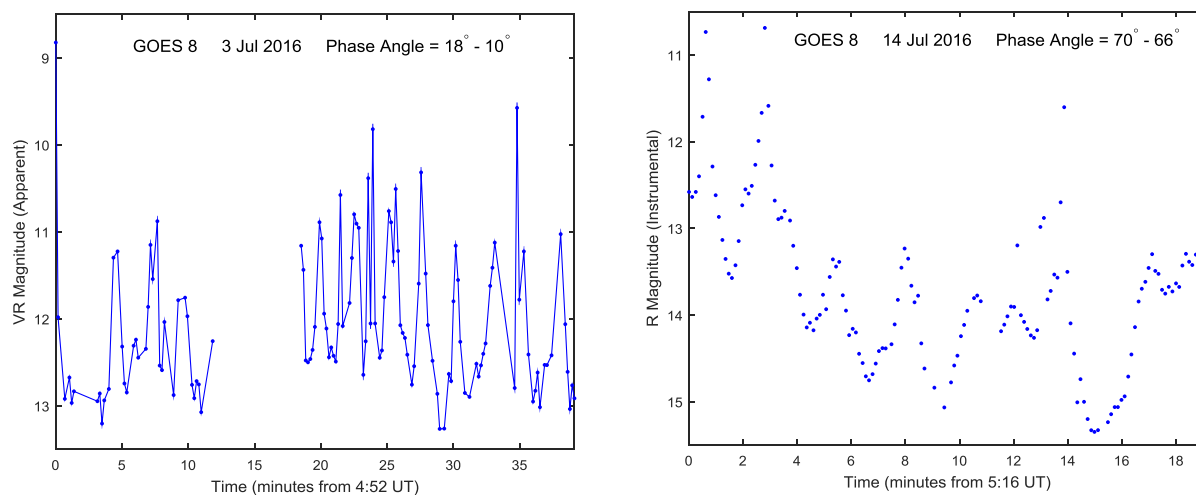


Fig. 6. July 2016 GOES 8 light curves (*left*: Lowell 1.1 m Hall *right*: Lowell 1.8 m Perkins)

The most recent GOES 8 light curve was obtained on 19 April 2018 with the MRO 2.4 m telescope (see Fig. 7). These data were collected using a Bessel R and processed in the same fashion as the previous MRO observations except that they were calibrated to apparent R magnitude. The high frequency of this light curve suggests rapid rotation but there is no clearly visible periodicity.

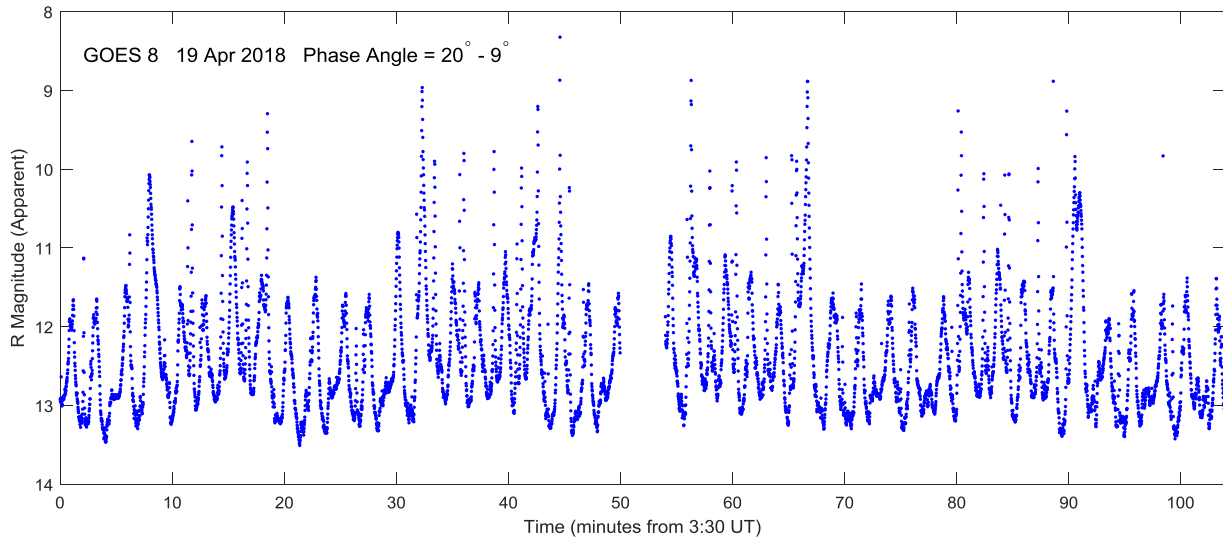


Fig. 7. 19 April 2018 GOES 8 light curve (MRO 2.4 m)

An intriguing result is obtained when the 19 April 2018 light curve is phase folded over a large range of candidate periods. In Fig. 8, the data are folded on the minimum dispersion period of 24.31 min, showing clear repetition in the 10 broad peaks and many of the sharper glints (particularly at 2, 11, and 14 minutes of phase). While there are differences in peak amplitudes and misaligned glints, these are not unexpected for uniform rotation given the varying geometry. The clean folding suggests that the satellite could be in uniform rotation with a 24.31 min spin period. On the other hand, all previous periodic GOES 8 and GOES 10 light curves have had no more than four broad peaks per rotation [2,3]. This light curve would have at least 10.

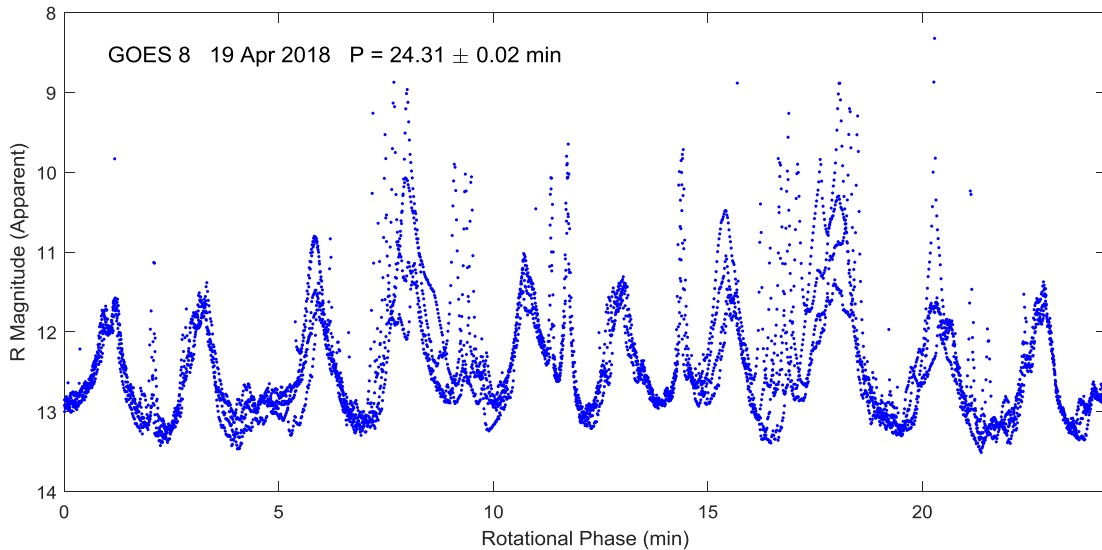


Fig. 8. Phase folded 19 April 2018 GOES 8 light curve

4. TORQUE-FREE TUMBLING DYNAMICS

To hopefully extract quantitative information from the ensemble of GOES 8 light curves and gain better insight into the satellite's evolving spin state, we will utilize rigid body rotational dynamics. For the remainder of the paper, we will assume that GOES 8's dynamics can be well approximated by torque-free rigid body rotation over the duration of a given light curve arc. While the satellite is constantly affected by solar radiation and other perturbations, these effects are likely negligible over a 1-2 hour observation window. Under torque-free rigid body assumptions, the satellite's rotation is defined by two constant, fundamental quantities. These are its inertial rotational angular momentum vector \vec{H} and kinetic energy T given by,

$$\vec{H} = NB[I]\vec{\omega} \quad T = \frac{1}{2}\vec{\omega} \cdot [I]\vec{\omega}$$

Here $[I] = \text{diag}(I_l, I_s, I_i)$ is the satellite's moment of inertia matrix expressed in a body fixed principal axis frame where $I_l \leq I_i \leq I_s$ are the minor, intermediate, and major moments of inertia respectively. The inertia subscripts stand for long, intermediate, and short since a satellite's longest and shortest dimensions often align with its minimum and maximum inertia axes respectively. The ordering of inertias in $[I]$ is chosen to be consistent with the long axis 3-1-3 Euler angle set to be discussed. $\vec{\omega}$ is the satellite's instantaneous angular velocity vector expressed in this principal axis frame, and NB is the rotation matrix from the body to the inertial frame. Two additional fundamental quantities are the dynamic moment of inertia I_d and effective spin rate ω_e which are given by,

$$I_d = \frac{H^2}{2T} \quad \omega_e = \frac{2T}{H}$$

where $H = \sqrt{\vec{H} \cdot \vec{H}}$. Equivalently, one write these equations as $H = I_d \omega_e$ and $T = \frac{1}{2} I_d \omega_e^2$.

I_d is limited to the range $I_l \leq I_d \leq I_s$. For $I_d = I_s$ or $I_d = I_l$ the satellite is in uniform rotation about the major or minor principal axis respectively. A tumbling object subject to internal energy dissipation will tend towards uniform rotation about the major axis, the minimum energy state for a given angular momentum. Rotation states where $I_l < I_d < I_i$ are referred to as long axis modes (LAM) because $\vec{\omega}$ precesses on a periodic, closed path about the satellite's minor inertia axis. For $I_i < I_d < I_s$, the motion is called a short axis mode (SAM) since $\vec{\omega}$ precesses instead about the satellite's major axis. When $I_d = I_i$, the satellite either spins about the intermediate axis or $\vec{\omega}$ asymptotically approaches the intermediate axis along the separatrix dividing the LAM and SAM regions. All intermediate axis and separatrix motion is dynamically unstable. Fig. 9 shows a variety of these closed $\vec{\omega}$ curves for different values of I_d projected onto the unit sphere. The separatrices are denoted by black curves. Ultimately, given $I_l, I_i,$ and I_s and either H and T or I_d and ω_e , the nature of the satellite's motion (i.e. the $\vec{\omega}$ curve) is known. All that is needed to form a complete angular velocity and attitude solution at given epoch are two initial phasing parameters and two angles defining the direction of \vec{H} . See References [9,10] for discussion of these complete solutions.

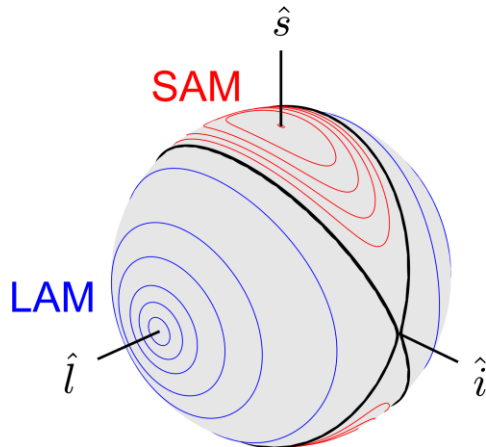


Fig. 9. Torque-free body frame angular velocity curves for GOES 8 end of life inertias projected onto the unit sphere (\hat{l} , \hat{i} , and \hat{s} are the minor, intermediate, and major inertia axes respectively)

For torque-free rigid body rotation, the satellite's motion can also be described by two constant inertial periods [10,11]. With the satellite's minimum inertia axis initially aligned with \vec{H} , the body frame is sequentially rotated through the precession ϕ , nutation θ , and rotation ψ angles according to the 3-1-3 (ϕ - θ - ψ) Euler angle set [10]. In this long axis convention, $P_{\bar{\phi}}$ is the average precession period of the long axis about \vec{H} and P_{ψ} is the rotation period of the long axis about itself. The nutation period P_{θ} is always proportional to P_{ψ} , so only $P_{\bar{\phi}}$ and P_{ψ} are independent [10]. These fundamental periods are illustrated in Fig. 10. The time required for ϕ to go through 360° (i.e. the true precession period) is not constant in general, resulting in aperiodic motion. For GOES 8 though, I_i and I_s are nearly equivalent so its motion approaches the classic axisymmetric "rolling cone" case where the true precession period is constant. $P_{\bar{\phi}}$ and P_{ψ} can be calculated given I_d , ω_e and the principal inertias. See the Appendix for the long axis convention periods for LAMs and SAMs.

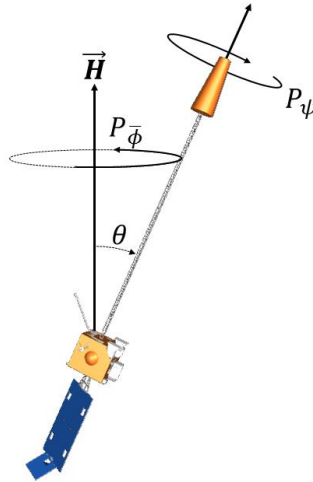


Fig. 10. Long axis convention fundamental tumbling periods

It is important to note that the ratio $P_{\psi}/P_{\bar{\phi}}$ is only a function of the GOES 8's principal inertias and I_d . $P_{\psi}/P_{\bar{\phi}}$ is plotted vs. I_d in Fig. 11 using GOES 8's end of life principal moments of inertia (provided by John Tsui, NOAA).

$$[I]_{GOES\ 8} = \begin{bmatrix} I_i & 0 & 0 \\ 0 & I_s & 0 \\ 0 & 0 & I_l \end{bmatrix} = \begin{bmatrix} 3440.9438 & 0 & 0 \\ 0 & 3561.0894 & 0 \\ 0 & 0 & 980.5133 \end{bmatrix} \text{ kg} \cdot \text{m}^2$$

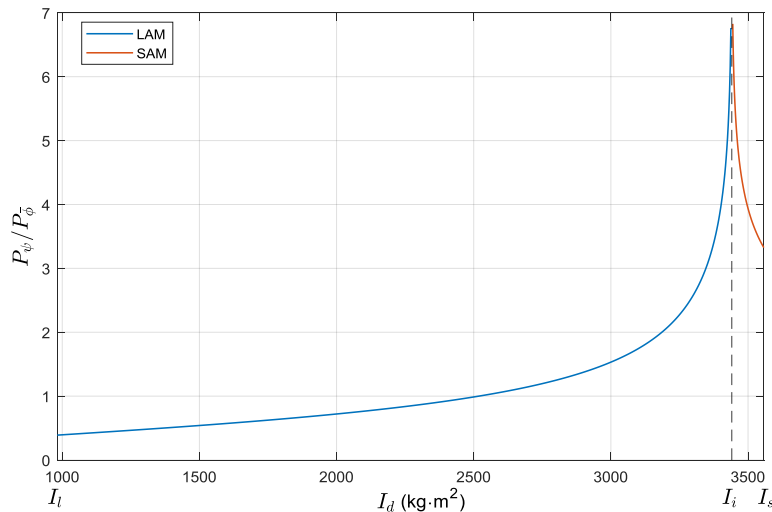


Fig. 11. GOES 8 fundamental tumbling period ratio $P_{\psi}/P_{\bar{\phi}}$ vs. dynamic moment of inertia I_d

There are several important points to make about Fig. 11. First, not all period ratios are physically possible [10]. For LAMs, $P_\psi/P_{\bar{\phi}} \geq 0.389$. For SAMs, $P_\psi/P_{\bar{\phi}} \geq 3.299$. These minimum ratios correspond to uniform rotation about the extremal principal axes. Considering the inversion problem, Fig. 11 also shows the potential ambiguity in I_d . To solve for I_d given $P_{\bar{\phi}}$, P_ψ , and the principal inertias, one must specify (or assume) whether the satellite is in LAM or SAM when $P_\psi/P_{\bar{\phi}} \geq 3.299$. For smaller ratios, only LAMs are possible. With this information, one can use the bisection method to calculate I_d [12]. ω_e can then be found from either period equation. Finally, as I_d approaches I_i from either direction, $\bar{\omega}$ takes an infinite amount of time to traverse the separatrix. P_ψ is also the period for $\bar{\omega}$ to make one cycle along its closed curve, so near the separatrix, P_ψ and therefore $P_\psi/P_{\bar{\phi}}$ go off to infinity.

Since GOES 8's true precession period is virtually constant given its moments of inertia, the satellite will return to nearly the same inertial attitude in constant intervals. This interval is called the "quasi-period" \bar{P} and is given by,

$$\bar{P} \approx mP_{\bar{\phi}} \approx nP_\psi$$

where m and n are integers such that $P_\psi/P_{\bar{\phi}} \approx m/n$. Ultimately, any period ratio can be approximated to arbitrary precision by a rational number (although m , n and therefore \bar{P} may be very large). Consequently, the motion will eventually repeat given enough time.

5. SIMULATED LIGHT CURVE MODEL

In order to explore how these fundamental periods manifest themselves in tumbling light curves and test candidate spin states, a light curve simulator was needed. Given the complexity of the observed light curves, a model was desired that could generate specular, glossy, and diffuse reflections as well as shadows and indirect illumination (i.e. multi-bounce reflections). So a light curve simulator was developed in NASA Goddard Space Flight Center's Freespace dynamics toolbox using the built in stochastic (Monte Carlo) ray tracer [13]. The three channel (red, green, blue) ray tracer employs a bidirectional reflection distribution function (BRDF) based on the model by Ashikhmin and Shirley [14]. This energy conserving BRDF can generate diffuse, glossy, and specular reflections through a microfacet formulation to simulate small-scale surface roughness.

Another important aspect of the light curve simulator was an accurate GOES shape model. An existing model was updated to include an articulating solar array and trim tab. End of life orientations for these surfaces were provided by John Tsui of NOAA's satellite operations office. With the various surface materials of the GOES satellites well documented [7], their reflective properties in each color band were set to plausible pre-launch values. However, the true properties have likely been altered by space weathering effects. The bus and solar sail are covered in multi-layer insulation (MLI) and aluminized Kapton, materials that generate almost exclusively specular/glossy reflections. So macroscopic roughness was added to these surfaces better match the true material appearance and observed light curves. A ray traced image of the GOES shape model is shown in Fig. 12 and illustrates the complex reflections and shadows possible with the light curve simulator. The surface roughness of the bus MLI is also visible.

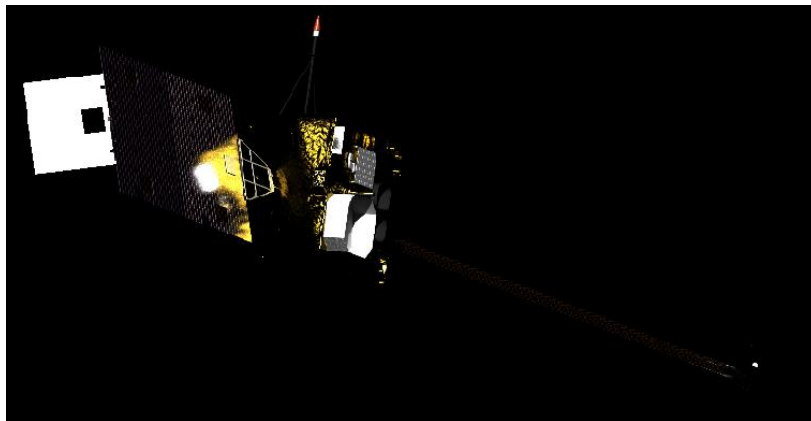


Fig. 12. Ray traced image of GOES 8 shape model rendered with Freespace light curve simulator

To generate more accurate simulated data and facilitate comparison with observed light curves, the correct time-varying positions of the satellite, sun, and earth-based observer were accounted for. The satellite's orbit was propagated from two line element (TLE) data obtained from the Joint Space Operations Center's Space-Track database. JPL ephemerides were used to determine the correct sun and earth positions. Finally, WGS 84 coordinates were used for the observation sites to obtain accurate viewing geometry. The raw output of the ray tracer is an image with three radiance values per pixel (one for each waveband). The simulated photometry was determined by integrating the radiance values ($\text{W}/\text{m}^2/\text{sr}$) over all pixels in the image and multiplying by each pixel's solid angle. Each of the three radiance values was pre-multiplied by the prescribed photometric filter's average transmittance in that waveband. This yielded a total irradiance (W/m^2) at the observing location. Finally, this irradiance value was calibrated to the prescribed filter's corresponding zero point flux and converted to magnitudes. Successive reduced images were then stacked chronologically to generate a simulated light curve.

6. SIMULATED LIGHT CURVE SURVEYS

We will now show results of two simulated light curve surveys conducted with the Freespace light curve simulator and high fidelity GOES 8 model. For each survey, a range of LAM, SAM, and uniform spin states were explored. For each spin state, 400-500 runs were conducted, randomly sampling the satellite's angular momentum vector (pole) over the sphere of inertial directions to obtain different viewing aspects.

6.1 Inertial Observation

The first survey assumed inertially fixed viewing and lighting geometry so that all light curve variation was due solely to the satellite's rotation state. The sun-satellite-observer phase angle was set to 30° , similar to the geometry for many of the above observations. Fig. 13 shows a sample light curve from this survey in a SAM rotation state with $P_{\bar{\phi}} = 3.16$ min and $P_{\psi} = 11.59$ min. The structure is similar to the 28 September 2015 and 19 April 2018 data with a 4-5 mag variation in brightness and sharp, regularly spaced peaks. The light curve's normalized Fourier power spectrum reveals that the dominant light curve frequencies are integer linear combinations of the tumbling fundamental frequencies. The power spectra of tumbling asteroids are known to be dominated by these linear combinations [10,11]. Fig. 14 shows the ensemble of power spectra for these 400 inertial SAM runs and all notable frequencies correspond to fundamental frequency combinations (some of which have been left unlabeled for clarity). Multiples of the long axis precession frequency $f_{\bar{\phi}}$ dominate the power spectra. This is further illustrated in Fig. 15 where histograms of the two largest amplitude frequencies for each light curve are plotted. We see that multiples of $f_{\bar{\phi}}$, particularly even ones, are almost always present. It is useful to note that the largest peak never has a frequency higher than $4f_{\bar{\phi}}$. This is also the maximum precession harmonic seen in previously observed periodic GOES light curves [2]. It was found that the bus and solar sail generated the majority of reflections given their highly reflective and crinkled surfaces. Solar array and trim tab glints were much less frequent due to their near mirror-like finish.

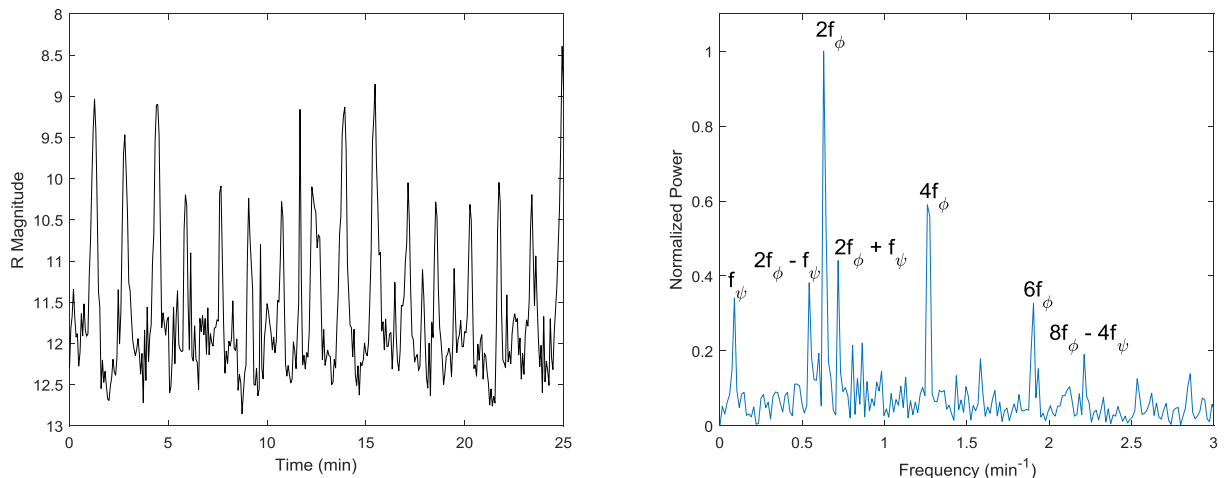


Fig. 13. Simulated GOES 8 Light Curve and Corresponding Fourier Power Spectrum (Inertial $I_d = 3520 \text{ kg}\cdot\text{m}^2$ SAM $P_{\bar{\phi}} = 3.16$ min $P_{\psi} = 11.59$ min)

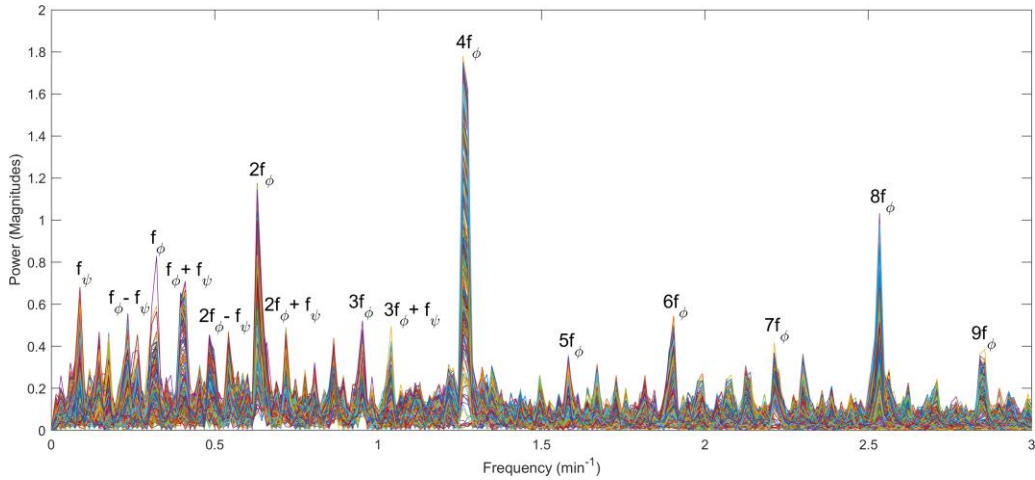


Fig. 14. Ensemble Power Spectra and Corresponding Fundamental Frequency Combinations (Inertial $I_d = 3520 \text{ kg}\cdot\text{m}^2$ SAM $P_{\bar{\phi}} = 3.16 \text{ min}$ $P_{\psi} = 11.59 \text{ min}$, 400 runs over celestial sphere)

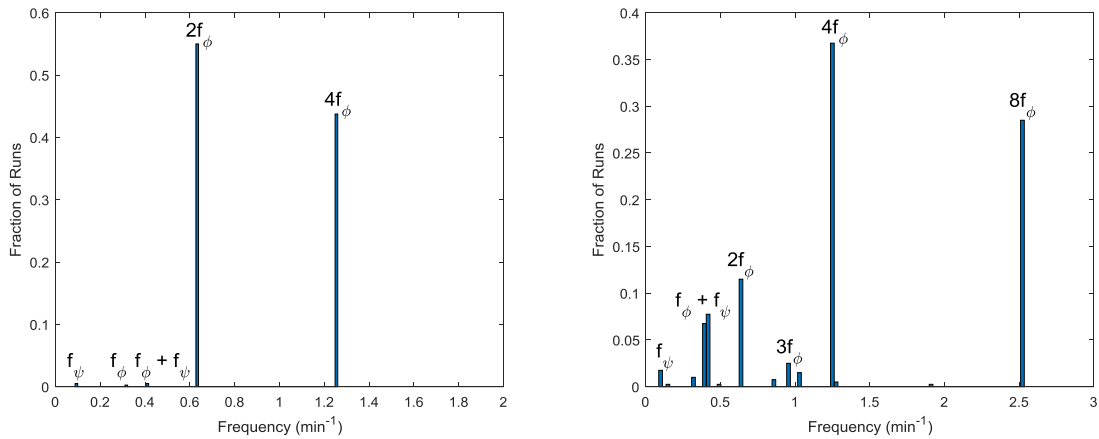


Fig. 15. Histograms of Largest (*left*) and 2nd Largest (*right*) Amplitude Frequencies in each Light Curve (Inertial $I_d = 3520 \text{ kg}\cdot\text{m}^2$ SAM $P_{\bar{\phi}} = 3.16 \text{ min}$ $P_{\psi} = 11.59 \text{ min}$, 400 runs over celestial sphere)

Fig. 16 shows dominant frequency histograms for a LAM case with $P_{\bar{\phi}} = 4.89 \text{ min}$ $P_{\psi} = 4.09 \text{ min}$. This state corresponds to θ of 62° , somewhat far from uniform rotation ($\theta = 90^\circ$). For LAMs, the influence of P_{ψ} on the light curve structure should be greater. Nevertheless, Fig. 16 shows that even for this energetic LAM case, $f_{\bar{\phi}}$ dominates.

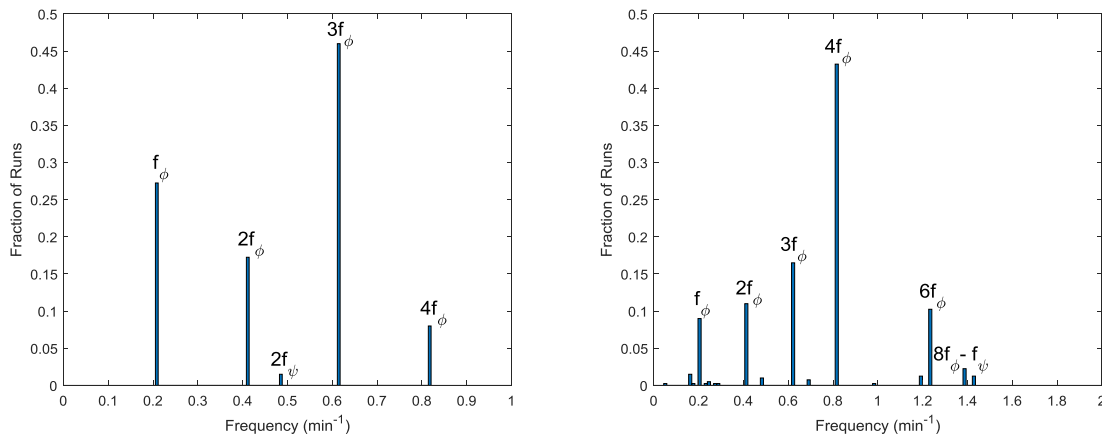


Fig. 16. Histograms of Largest (*left*) and 2nd Largest (*right*) Amplitude Frequencies in each Light Curve (Inertial $I_d = 2250 \text{ kg}\cdot\text{m}^2$ LAM $P_{\bar{\phi}} = 4.89 \text{ min}$ $P_{\psi} = 4.09 \text{ min}$, 400 runs over celestial sphere)

Although not shown, several other inertial cases for I_d values between these LAM and SAM states were considered. The trend continued for these cases, with a multiple of $f_{\bar{\phi}}$ almost exclusively the largest amplitude frequency.

6.2 GEO Observation

We will now discuss the second simulated light curve survey which account for GOES 8's orbit and the earth fixed observer. For this survey, ~110 min observation arcs were taken which covered a phase angle variation of $49^\circ - 27^\circ$. The first case tested was uniform rotation to see how much the periodic light curve structure would be skewed by relative motion. Fig. 17 shows the ensemble power spectra for 500 runs with a uniform rotation period of $P_{\bar{\phi}} = 14.46$ min and random spin poles. We see that all power is concentrated at multiples of the rotation frequency, nearly identical to what is expected for an ideal, inertially fixed case. The only notable difference is that there is a low frequency alias peak in many of these GEO power spectra due to the slowly changing phase angle.

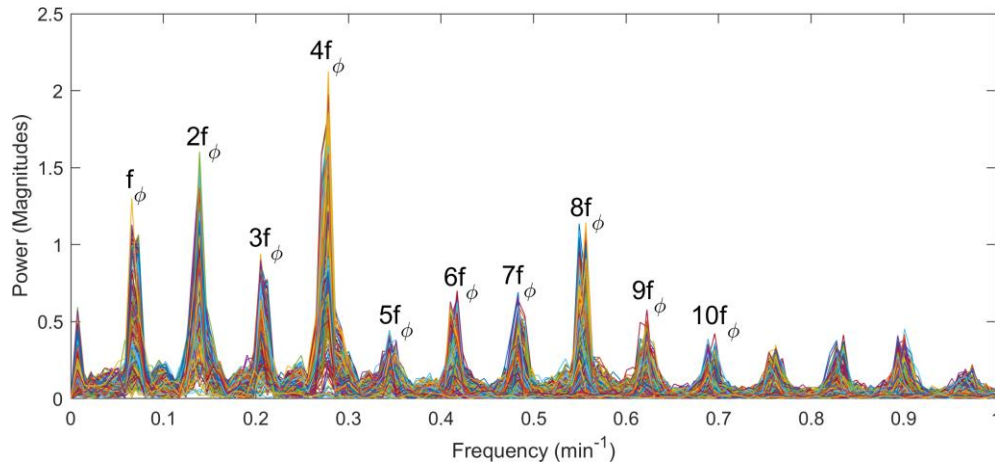


Fig. 17. Ensemble Power Spectra and Corresponding Rotation Period Harmonics (GEO Uniform $P_{\bar{\phi}} = 14.46$ min, Phase angle: $49^\circ - 27^\circ$, 500 runs over celestial sphere)

To better understand the effects of relative motion one should expect in GEO observations, the error between the observed (synodic) precession period $P_{\bar{\phi}}^{syn}$ and the true period $P_{\bar{\phi}}$, $\Delta P_{\bar{\phi}} = P_{\bar{\phi}}^{syn} - P_{\bar{\phi}}$, were quantified for several cases. Reference [8] discusses that ΔP for uniform rotation is driven by the time rate of change of the phase angle bisector (PAB), the average between the satellite to sun and satellite to observer directions. For PAB variation exclusively in a uniformly rotating satellite's equatorial plane, ΔP is estimated by the following equation,

$$\Delta P = \frac{d(PAB)}{dt} P_{syn}^2$$

where P_{syn} is the observed synodic period. The magnitude of ΔP decreases if the PAB motion is mostly in satellite body frame latitude and increases if the motion is mostly in longitude at a non-zero latitude. ΔP is positive or negative if the PAB moves with or against the satellite's rotation respectively. For relatively low inclination GEO objects, $d(PAB)/dt$ is approximately one half of earth's sidereal spin rate (i.e. $\sim 3.48e^{-4} \text{ min}^{-1}$). This estimate was tested for uniform rotation with $P_{\bar{\phi}} = 14.46$ min where ΔP should be roughly 4.4 s for this period. 500 light curves with GEO observing conditions and random poles were folded over their respective $P_{\bar{\phi}}^{syn}$, taken to be the minimum dispersion phase folded period. Two examples light curves are plotted in Fig. 18 and reveal very limited dispersion in peak alignment but notable variability in successive peak amplitudes.

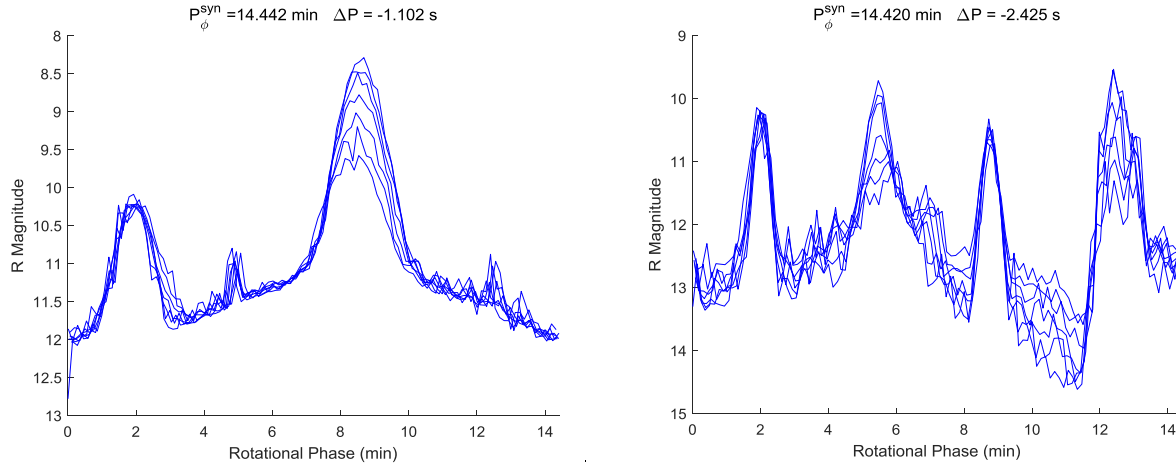


Fig. 18. Phase Folded Light Curves with Dominant Frequencies of 2 and $4f_{\bar{\phi}}$
(GEO Uniform $P_{\bar{\phi}} = 14.46$ min, Phase angle: 49° - 27°)

Fig. 19 shows that the majority of $\Delta P_{\bar{\phi}}$ values for these 500 runs are within ± 5 s, agreeing with the ~ 4.4 s estimate calculated above. Outlying values were mostly obtained for spin poles near earth's equator where the PAB motion is at high latitudes.

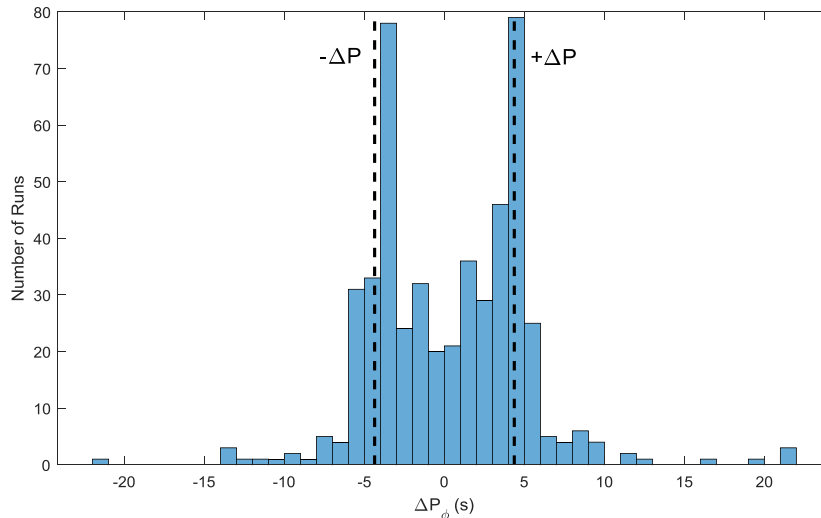


Fig. 19. Distribution of $\Delta P_{\bar{\phi}}$ for Uniform Rotation with $P_{\bar{\phi}}^{syn}$ Provided by Minimum Dispersion Phase Folding
(GEO Uniform $P_{\bar{\phi}} = 14.46$ min, Phase angle: 49° - 27° , 500 runs over celestial sphere)

Moving on to complex rotation cases, Fig. 20 shows a simulated SAM light curve with $P_{\bar{\phi}} = 7.04$ min $P_{\psi} = 25.83$ min. These observations clearly show a decrease in mean magnitude due to the changing phase angle. The lowest frequency peak in the corresponding power spectrum is most likely an alias due to this decrease in mean magnitude. The remaining dominant power spectrum peaks still coincide with linear combinations of the two sidereal tumbling frequencies combinations albeit with slight differences due to the relative motion.

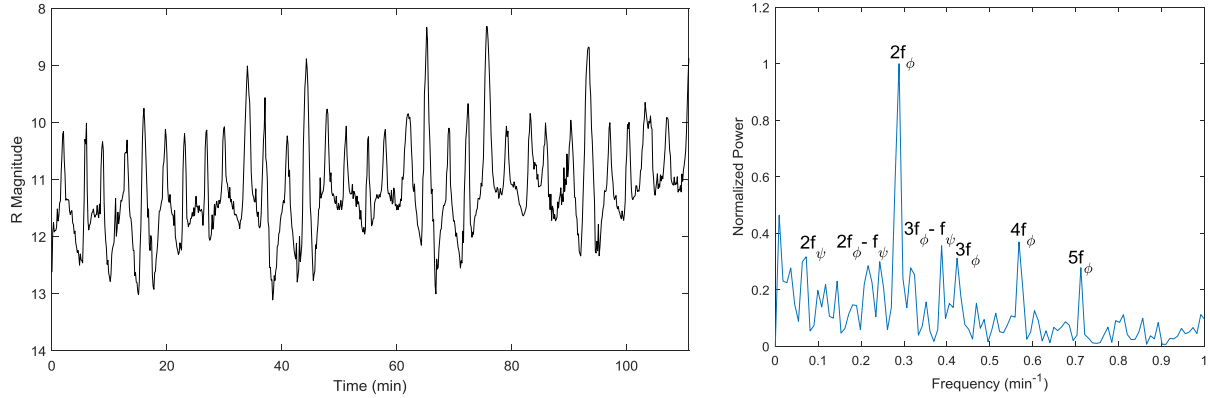


Fig. 20. Simulated Light Curve and Corresponding Fourier Power Spectrum (GEO $I_d = 3520 \text{ kg}\cdot\text{m}^2$ SAM $P_{\bar{\phi}} = 7.04 \text{ min}$ $P_{\psi} = 25.83 \text{ min}$, Phase angle: $49^\circ\text{-}27^\circ$)

To quantify the synodic affects for tumbling motion, $\Delta P_{\bar{\phi}}$ was calculated for the Fig. 20 light curve. The precession motion for this SAM state is very similar to uniform rotation where $\Delta P_{\bar{\phi}}$ according the above equation would be $\pm 1 \text{ s}$ for $P_{\bar{\phi}} = 7.04 \text{ min}$. Given the power spectrum's limited frequency resolution in Fig. 20, iterated Fourier series fits were used to more accurately estimate $P_{\bar{\phi}}^{\text{syn}}$. Initial guesses for the Fourier series component frequencies and coefficients were taken from the Fig. 20 power spectrum and the fit was iterated until convergence using linearized least squares. A Fourier series solution with 9 component frequencies for the Fig. 19 light curve is provided in Fig. 21. This solution provided $P_{\bar{\phi}}^{\text{syn}} = 7.01 \text{ min}$ or a $P_{\bar{\phi}}^{\text{syn}} - P_{\bar{\phi}}$ difference $\Delta P_{\bar{\phi}}$ of -1.77 s . This is slightly larger than the equatorial value because satellite's pole was roughly in earth's equatorial plane (-14° latitude) with the PAB moving at a non-zero body frame latitude. Two other light curves from the above SAM search showed similar consistency with $\Delta P_{\bar{\phi}}$ of -0.98 s and 1.04 s for poles with equatorial latitudes of 89° and -89° respectively (consistent with the sign of ΔP differing for prograde and retrograde satellite rotation. Overall, for $P_{\bar{\phi}} = 7 \text{ min}$ these $\Delta P_{\bar{\phi}}$ errors are quite small ($<1\%$).

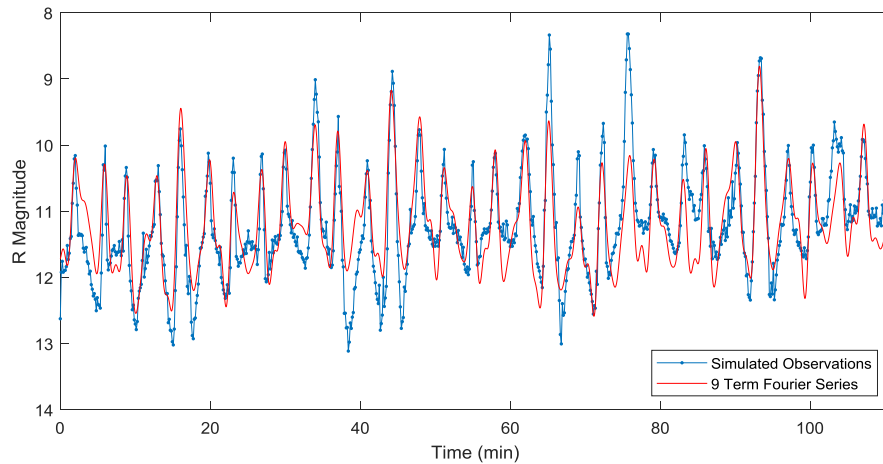


Fig. 21. Simulated Light Curve and Iterated Fourier Series Fit Informed by Power Spectrum (GEO $I_d = 3520 \text{ kg}\cdot\text{m}^2$ SAM $P_{\bar{\phi}} = 7.04 \text{ min}$ $P_{\psi} = 25.83 \text{ min}$, Phase angle: $49^\circ\text{-}27^\circ$)

Interestingly, Fig. 22 shows that the histograms of dominant frequencies for this time-varying geometry SAM $P_{\bar{\phi}} = 7.04 \text{ min}$ $P_{\psi} = 25.83 \text{ min}$ case are very comparable to those for the inertially fixed case with the same I_d in Fig. 15. The largest amplitude frequency in each light curve is almost always 2 or $4f_{\bar{\phi}}$ and the second largest peak is most often a multiple of $f_{\bar{\phi}}$ as well. The ensemble power spectra for the two cases are also similar with the notable exception for the time-varying case in Fig. 23 being the spurious peaks at $\sim 0.01 \text{ min}^{-1}$ due to changing phase.

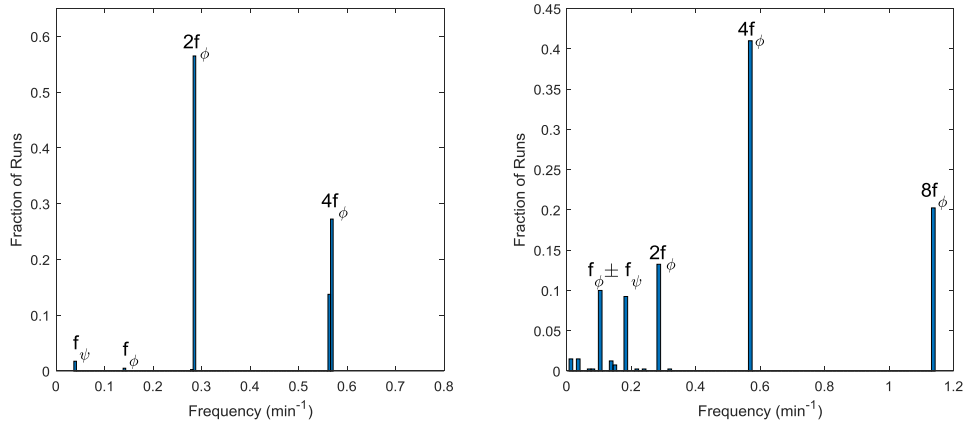


Fig. 22. Histograms of Largest (*left*) and 2nd Largest (*right*) Amplitude Frequencies in each Light Curve (GEO $I_d = 3520 \text{ kg}\cdot\text{m}^2$ SAM $P_{\bar{\phi}} = 7.04 \text{ min}$ $P_{\psi} = 25.83 \text{ min}$, Phase angle: $49^\circ\text{-}27^\circ$, 400 runs)

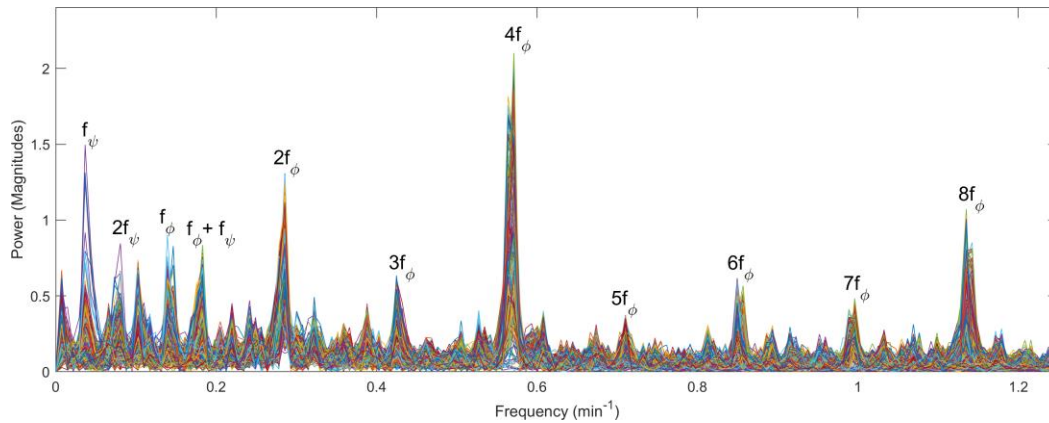


Fig. 23. Ensemble Power Spectra and Corresponding Fundamental Frequency Combinations (GEO $I_d = 3520 \text{ kg}\cdot\text{m}^2$ SAM $P_{\bar{\phi}} = 7.04 \text{ min}$ $P_{\psi} = 25.83 \text{ min}$, Phase angle: $49^\circ\text{-}27^\circ$, 400 runs)

Increasing the tumbling periods for the SAM $I_d = 3520 \text{ kg}\cdot\text{m}^2$ case to $P_{\bar{\phi}} = 15.08 \text{ min}$ and $P_{\psi} = 55.34 \text{ min}$, the resulting ensemble power spectra are plotted in Fig. 24. Here we see that multiples of $f_{\bar{\phi}}$ still dominate the light curves. Also, since $f_{\psi} < f_{\bar{\phi}}/3.3$ for SAMs, harmonics involving f_{ψ} have been pushed down below $2f_{\bar{\phi}}$ where they can be obscured by the long period phase change aliasing. This illustrates that identifying f_{ψ} for longer period complex rotation can be difficult, especially for tumbling light curves with negligible f_{ψ} contributions.

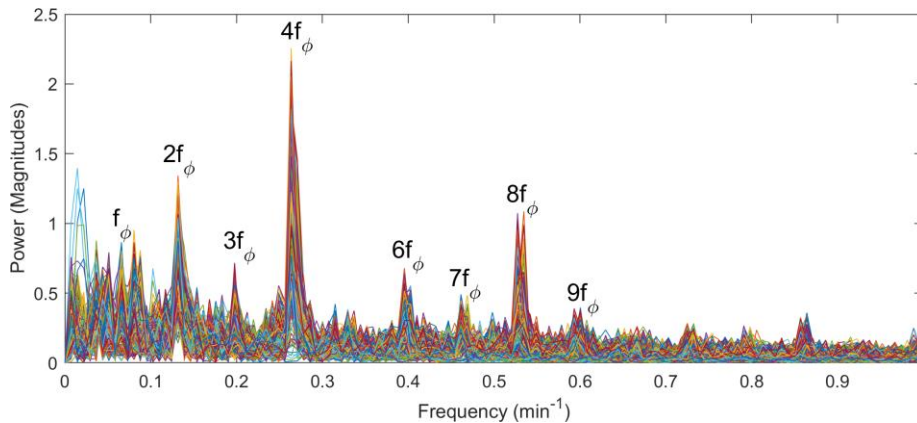


Fig. 24. Ensemble Power Spectra and Corresponding Fundamental Frequency Combinations (GEO $I_d = 3520 \text{ kg}\cdot\text{m}^2$ SAM $P_{\bar{\phi}} = 15.08 \text{ min}$ $P_{\psi} = 55.34 \text{ min}$, Phase angle: $49^\circ\text{-}27^\circ$, 400 runs)

The final case tested for realistic GEO observing conditions was quasi-periodicity. A SAM state with $P_{\bar{\phi}} = 4.43$ min $P_{\psi} = 15.55$ min ($P_{\psi}/P_{\bar{\phi}} = 3.51 \sim 7/2$) was tested. Fig. 25 shows a sample light curve folded on the corresponding synodic quasi-period of 30.85 min ($7P_{\bar{\phi}} = 31.01$ min). The light curve covers roughly 3.5 quasi-periods and almost exactly repeats, demonstrating that the satellite periodically returns to nearly the same attitude.

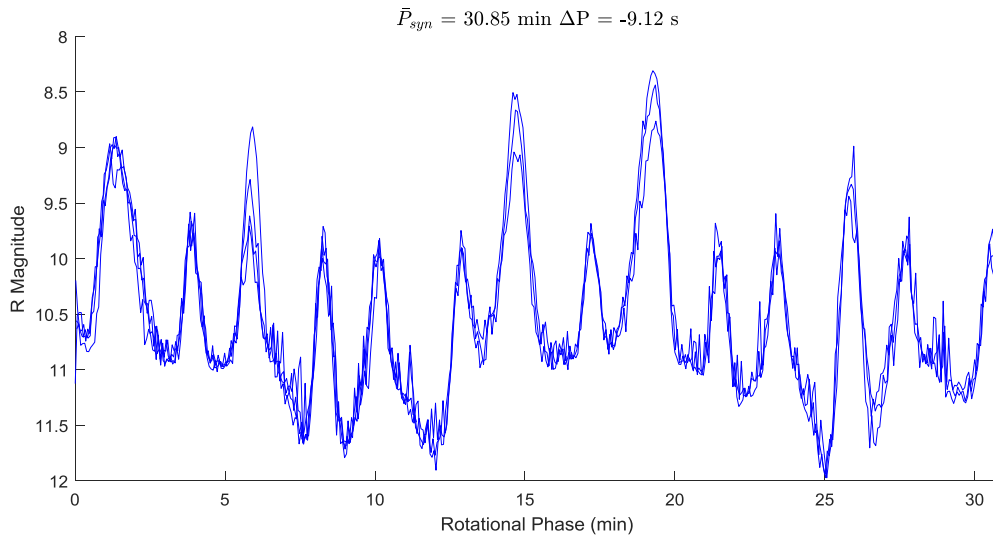


Fig. 25. Tumbling GOES 8 Light Curve Folded on Quasi-period
(GEO $I_d = 3535$ kg·m² SAM $P_{\bar{\phi}} = 4.43$ min $P_{\psi} = 15.55$ min, Phase angle: 20° - 9°)

Overall, the simulated light curve surveys provided a number of insights. First of all, integer linear combinations of the tumbling fundamental frequencies $f_{\bar{\phi}}$ and f_{ψ} account for the overwhelming majority of observed light curve frequencies. Furthermore, for all anticipated energy levels (SAMs and high I_d LAMs), multiples of the precession frequency $f_{\bar{\phi}}$ dominate the power spectra with three or more different multiples often observed. This is likely due in part to the large, axisymmetric solar sail which provides frequent precessional reflections but is unaffected by long axis rotation (i.e. f_{ψ}). As a further constraint, the most dominant frequency in any simulated light curve was never higher than $4f_{\bar{\phi}}$, likely constrained by the cube-shaped bus and solar sail not providing more than four broad reflections per precession period. For GEO observing conditions with slowly time-varying phase and viewing geometry, the dominant light curve frequencies still closely agreed with tumbling frequency combinations apart from low frequency phase change aliases sometimes included. Predicted differences between synodic and sidereal precession periods were found to be consistent with those observed for both uniform and complex rotation. These differences were less than 6 s for the majority of spin states with $P_{\bar{\phi}} < 15$ min. Finally, for slower complex rotation, the low frequency f_{ψ} terms were often obscured by long period phase change aliases or multiples of $f_{\bar{\phi}}$, making identification of mild tumbling rotation more difficult.

7. RESULTS

With valuable insight gained about GOES 8 light curve structure from the simulated observations, we will now extract candidate rotation states from the observations and validate them with simulated light curves to better understand the satellite's ongoing dynamical evolution.

7.1 12 September 2015

The dominant frequencies in the 12 September 2015 observations are shown in Table 1. The most dominant frequency is 0.119 min⁻¹. Given the light curve survey trends, this is mostly likely 1, 2, 3, or $4f_{\bar{\phi}}$. This frequency is unlikely to be $f_{\bar{\phi}}$ due to the second largest peak in part B. With energy dissipation, the satellite is most likely to be

in SAM where 2 or $4f_{\bar{\phi}}$ was almost exclusively the dominant frequency. Proximity to the 28 September 2015 observations with a clear 14.51 min period suggests that $0.119 \text{ min}^{-1} = 2f_{\bar{\phi}}$ or $P_{\bar{\phi}} \approx 16.8 \text{ min}$. This was also the minimum dispersion phase folded period, although there was significant variation over successive peak locations and amplitudes. Generating an ensemble of simulated light curves over the range of spin pole and phase angle assuming uniform rotation, the best solution is provided in Fig. 26. While the major peaks align well in time, the numerous glints, variable peak amplitudes, and notable increase in magnitude over time are not replicated by the best fit solution. These findings and the poor phase folding suggest that the satellite is actually in complex rotation with $P_{\bar{\phi}} \approx 16.8 \text{ min}$. Assuming the satellite is in SAM, $P_{\psi} \geq 3.3P_{\bar{\phi}}$. The $\sim 0.03 \text{ min}^{-1}$ frequency in Table 1 may be driven by a multiple of f_{ψ} or it may be due to the time-varying phase angle.

Table 1: Dominant Frequencies in 12 September 2015 Light Curve (min^{-1})

Part A. Iterated Fourier Series	Part B. Iterated Fourier Series	Part A and B Lomb-Scargle
0.1193	0.1187	0.1202
0.2327	0.1757	0.0307
0.3238	0.0321	0.2429

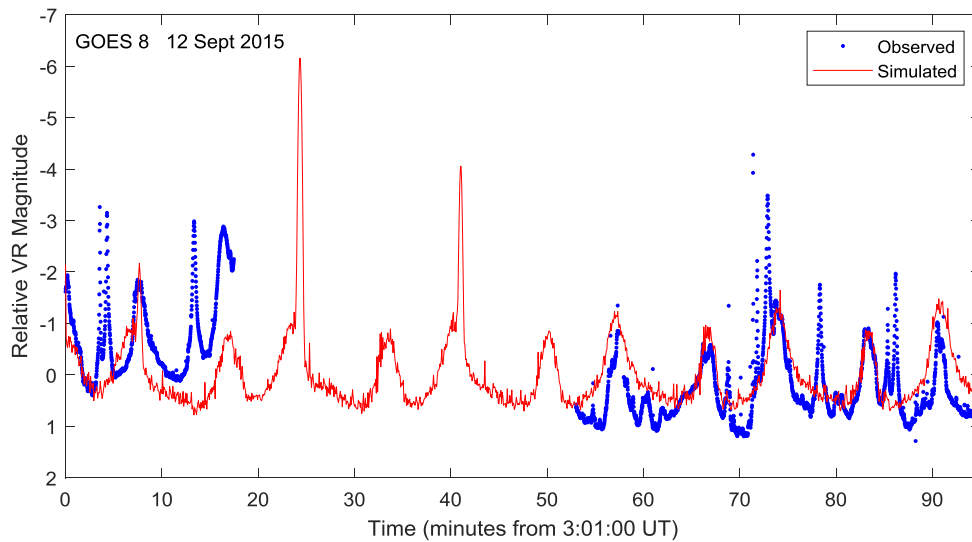


Fig. 26. Observed and Best-Fit Simulated 12 Sept 2015 Light Curves (Uniform Rotation with $P_{\bar{\phi}} = 16.75 \text{ min}$, Pole J2000 RA = 142° latitude = 8°)

7.2 28 September 2015

The 28 September 2015 observations exhibit very strong periodicity with a best-fit phase folded period of 14.46 min in Fig. 4. While there is some variability in the peak amplitudes over successive cycles, a number of simulated 28 September 2015 uniform rotation light curves with $P_{\bar{\phi}} = 14.46 \text{ min}$ showed similar dispersion when folded, including one time glints.

Power spectra of the first and second halves of the light curve were generated separately to avoid observation gap aliases. The frequency estimates were improved through iterative Fourier series fits. The power spectrum and converged Fourier series solution for part A of the light curve are shown in Fig. 27. The five largest power spectrum peaks were taken and iterated. The converged values for parts A and B as well as the top Lomb-Scargle periodogram frequencies for the entire light curve are provided in Table 2. All frequencies except the bolded ones are approximately multiples of 0.0695 min^{-1} (a period of $\sim 14.4 \text{ min}$). The two bolded frequencies are quite small and could be due to the long period mean magnitude variation. The clean phase folding, light curve survey findings, and multiples present in Table 2 strongly point to the dominant frequency of 0.2772 min^{-1} being $4f_{\bar{\phi}}$ (i.e. $P_{\bar{\phi}} \approx 14.46 \text{ min}$). Furthermore, with the strong periodicity and many observed multiples of $f_{\bar{\phi}}$, the satellite is likely in or quite close to uniform rotation.

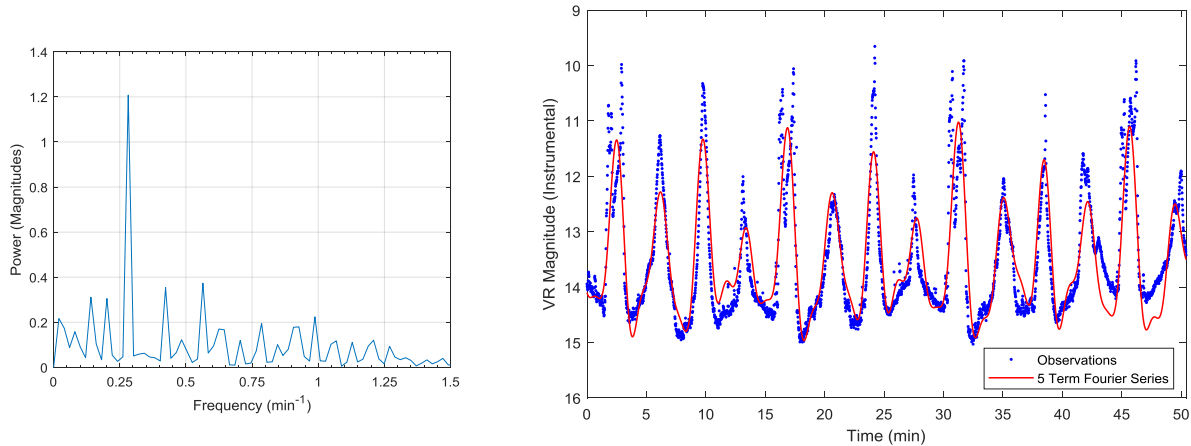


Fig. 27. 28 September 2015 Part A Power Spectrum and Iterated Fourier Series Fit

Table 2: Dominant Frequencies in 28 September 2015 Light Curve (min^{-1})

Part A Iterated Fourier Series	Part B Iterated Fourier Series	Part A and B Lomb-Scargle
0.2779	0.2772	0.2772
0.5564	0.06479	0.5544
0.4176	0.0321	0.009
0.2010	0.6127	0.2074

This candidate state was tested by generating simulated uniform rotation light curves with $P_{\bar{\phi}} = 14.46$ min. GOES 8's orbit was propagated to the light curve start time from the nearest TLE and the observer set at MRO's earth-fixed position. First, a blind random search over all possible spin poles and initial rotation phasing was conducted to find solutions with the lowest root mean square (RMS) residual compared to the observations. Only relative magnitudes were compared because the observations were not zero point calibrated and therefore included instrumental and extinction effects. The best-fitting blind solutions were then iterated using Nelder-Mead simplex optimization, letting $P_{\bar{\phi}}$, the pole, and the initial phasing vary. This allowed for discrepancies between the observed $P_{\bar{\phi}}^{\text{syn}}$ and $P_{\bar{\phi}}$ to hopefully be corrected.

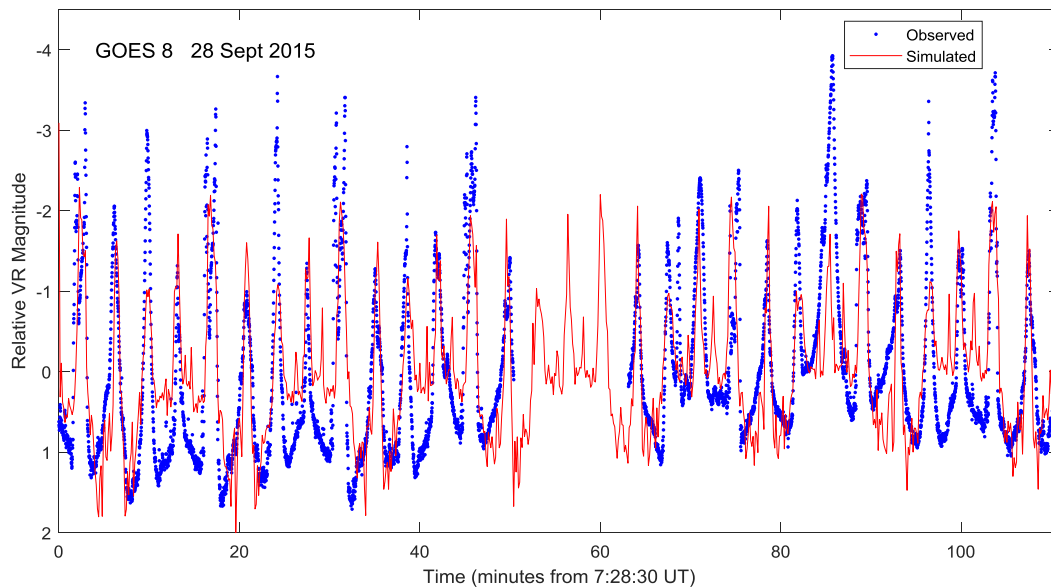


Fig. 28. Observed and Best-Fit Simulated 28 Sept 2015 Light Curves (Uniform Rotation with $P_{\bar{\phi}} = 14.51$ min, Pole J2000 RA = 155° latitude = -69°)

The best-fitting solution is provided in Fig. 28 with $P_\phi = 14.51$ min. This period and the nearly retrograde rotation are consistent with P_ϕ^{syn} being several seconds shorter. This solution fits the observed frequency evolution well with the majority of the simulated peaks closely aligned with the observations. The observed amplitudes are consistently larger than simulated, suggesting a discrepancy in reflective properties, spin pole, or mildly complex rotation. Close to uniform rotation, $P_\psi \approx 3.3P_\phi$ which would mean $P_\psi \approx 47.9$ min ($f_\psi \approx 0.0209$ min⁻¹). Such a low frequency, if present, could be obscured by the changing phase angle. Nevertheless, the bolded frequencies in Table 2 may in fact be due to multiples of f_ψ (0.0209 min⁻¹) which were commonly observed frequencies in the light curve surveys.

7.3 6 February 2016

The top iterated Fourier series and Lomb-Scargle frequencies for the 6 February 2016 observations are provided in Table 3. Given, the frequencies present and the well-fitting 14.51 precession period in 28 September 2015, the dominant 0.148 min⁻¹ frequency most likely corresponds to $2f_\phi$ (i.e. $P_\phi \approx 13.5$ min). Simulated uniform rotation light curves with $P_\phi = 13.51$ min fit the light curve periodicity well but did not replicate the observed increasing magnitude trend. Also, four of the dominant frequencies in Table 3 are not clearly related to this f_ϕ of 0.074 min⁻¹ suggesting the satellite is in complex rotation. For a mild SAM case near uniform rotation, $f_\psi \approx f_\phi/3.3$ (i.e. 0.022 min⁻¹). This would account for the remaining observed frequencies with 0.0204, 0.023 min⁻¹ $\approx f_\psi$, 0.051 min⁻¹ $\approx f_\phi - f_\psi$, and 0.112 min⁻¹ $\approx f_\phi + 2f_\psi$ all of which were commonly observed in the light curve surveys.

Table 3: Dominant Frequencies in 6 February 2016 Light Curve (min⁻¹)

Iterated Fourier Series	Lomb-Scargle
0.148	0.148
0.0232	0.0204
0.2195	0.051
0.3725	0.112

A simulated light curve search was conducted for the above SAM case with $P_\phi = 13.5$ min and $P_\psi = 45$ min and the correct time-varying 6 February 2016 observing geometry. The best-fitting case was slightly improved with Nelder-Mead simplex optimization, yielding the solution in Fig. 29. Here we see that the solution fits the observed light curve peak structure and decreasing amplitude trend well. The glints (likely off the trim tab or solar array) are not replicated, likely because they are highly sensitive to relative geometry.

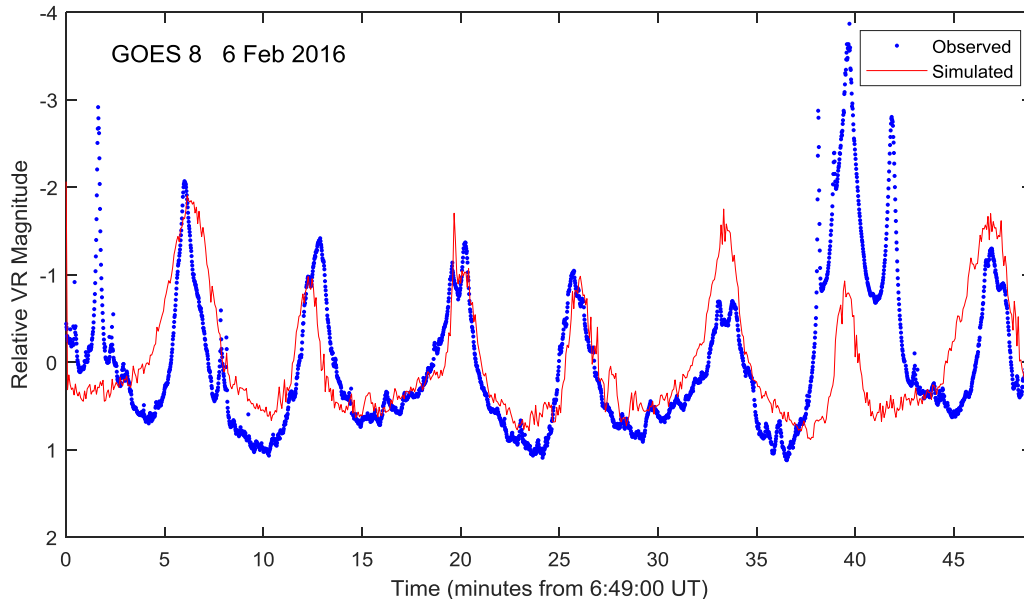


Fig. 29. Observed and Best-Fit Simulated 28 Sept 2015 Light Curves (SAM with $P_\phi = 13.51$ min $P_\psi = 45.01$ min, Pole J2000 RA = 126° latitude = 10°)

7.4 3 and 14 July 2016

While sparse, the 3 and 14 July 2016 observations do provide some insight into GOES 8's spin state evolution. The short 11 day span between these epochs suggests that their spin states should not differ considerably. Lomb-Scargle periodograms were generated for each light curves due to their observation gaps. These are provided in Fig. 30. They show that the light curves share statistically significant frequencies of 0.04, 0.1 and 0.4 min^{-1} . In addition, an iterated Fourier series fit to the 14 July observations showed dominant frequencies of 0.11, 0.37, and 0.22 min^{-1} . The 3 July observations also fold decently on a 25.6 min period, albeit with more than 10 broad peaks per cycle. With $4f_{\bar{\phi}}$ being the highest primary frequency observed in the light curve surveys, this 25.6 min period (or a multiple) is most likely a tumbling quasi-period. These findings suggest that $P_{\bar{\phi}}$ is either approximately 5 or 10 minutes at both epochs and the satellite is in complex rotation.

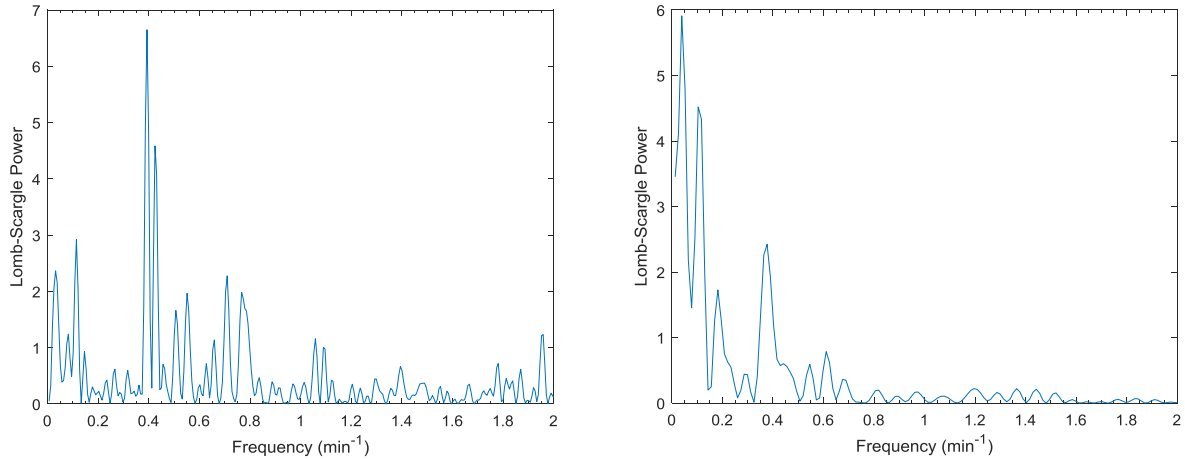


Fig. 30. Lomb-Scargle Periodograms for 3 and 14 July 2016 Light Curves

7.5 19 April 2018

The 19 April 2018 GOES 8 observations are the most detailed yet. Fig. 31 shows the power spectra for parts A and B of the light curve, again generated separately to avoid observation gap aliasing. Both power spectra show clearly dominant frequencies of 0.41 min^{-1} , 0.82 min^{-1} , 0.04 min^{-1} , and 0.12 min^{-1} .

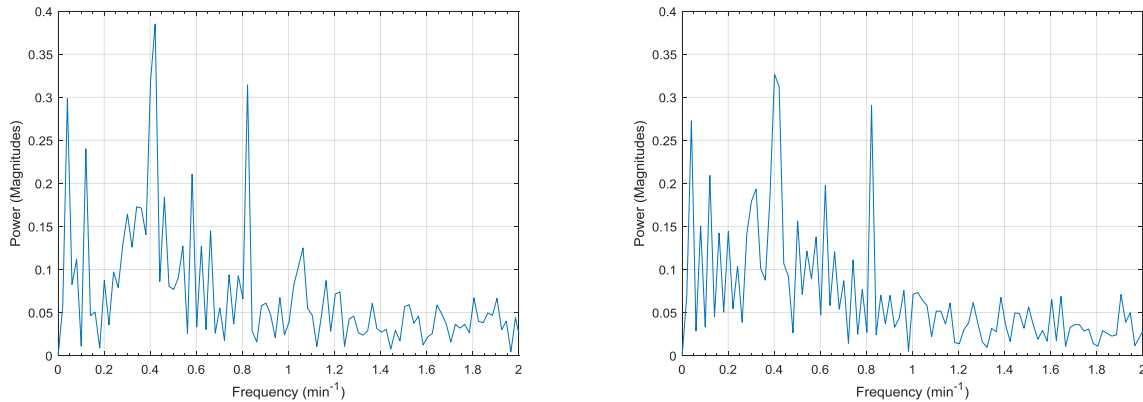


Fig. 31. 19 April 2018 Power Spectra (left: Part A right: Part B)

The top five iterated Fourier series frequencies are provided in Table 4 along with the top Lomb-Scargle frequencies for the entire light curve. All of the frequencies shown are approximately multiples of 0.041 min^{-1} . This common denominator corresponds to the 24.31 min best fold period from Fig. 8. Folding the observations on the next best-fitting periods of 4.88 min and 9.76 min showed significant variation in peak alignment. These facts alone would suggest that the satellite is in uniform rotation with a 24.31 min period. If this was the case, it would require the most dominant observed frequency to be $10f_{\bar{\phi}}$. But across the collection of simulated observations and previously

observed periodic GOES 8 light curves, the maximum dominant frequency ever observed for uniform or complex rotation was $4f_{\bar{\phi}}$. Given this valuable insight and the various frequencies present, it appears that the satellite is in complex rotation and the 24.31 min period is actually the tumbling quasi-period \bar{P} . To further confirm that the changing geometry did not skew underlying uniform rotation or generate a dominant peak of $10f_{\bar{\phi}}$, an ensemble of simulated light curves was generated over the 19 April 2018 arc for uniform rotation periods of 4.88 min, 9.76 min, and 24.31 min. None had notable variation in light curve peak phasing when folded. Also, no 24.31 min light curves showed more than four broad peaks per rotation.

Table 4: Dominant Frequencies in 19 April 2018 Light Curve (min^{-1})

Part A Iterated Fourier Series	Part B Iterated Fourier Series	Part A and B Lomb-Scargle
0.4112	0.4099	0.4112
0.8219	0.8212	0.8223
0.0406	0.0395	0.0409
0.1178	0.6145	0.1202
0.5758	0.1205	0.2909

As discussed above, $P_{\bar{\phi}}$ for GOES 8 is virtually constant given its shape. So in complex rotation, the satellite will return to nearly the same inertial orientation after \bar{P} determined by $P_{\psi}/P_{\bar{\phi}}$. Applying our survey findings, the 0.41 min^{-1} frequency is almost certainly 1,2,3, or $4f_{\bar{\phi}}$. Given the other frequencies present, 2 or $4f_{\bar{\phi}}$ are the most likely assignments, making $P_{\bar{\phi}} \approx 4.88$ min or 9.76 min. This would mean that $m = 5$ or 2.5 respectively. Given m for the 9.76 min period is not an integer, the satellite would be half a precession cycle off in 24.31 min and the light curve would likely not fold as cleanly. No clear improvement was made when folding the observed light curve on a 48.62 min period. As such, $P_{\bar{\phi}}$ was not likely to be 9.76 min. Unlike ϕ , the long axis rotation angle ψ will return to the same value in $P_{\psi}/2$ for SAMs except moving the opposite direction. So it is possible for a light curve to fold well on $nP_{\psi}/2$ where n is an integer. Therefore candidate P_{ψ} 's were calculated by dividing \bar{P} of 24.31 min by increments of 1/2. Select values are provided in Table 5 along with the resulting period ratios and possible modes.

Table 5: Select Candidate P_{ψ} Values for 19 April 2018 Light Curve ($P_{\bar{\phi}} = 4.88$ min, $\bar{P} = 24.31$ min)

n	0.5	1	1.5	2	3	4	5	6
P_{ψ}	48.62	24.31	16.21	12.15	8.10	6.07	4.88	4.05
$P_{\psi}/P_{\bar{\phi}}$	10	5	3.33	2.5	1.66	1.25	1	0.83
Possible Modes	LAM, SAM	LAM, SAM	LAM, SAM	LAM	LAM	LAM	LAM	LAM

Sets of simulated light curves were generated with the correct 19 April 2018 geometry for all of these candidate rotation states in addition to tumbling cases with $P_{\bar{\phi}} = 9.76$ min. As expected, the cases with $P_{\bar{\phi}} = 9.76$ min did not fold as cleanly on a 24.31 min period as the observations. Furthermore, when compared to the observations, the best-fitting $P_{\bar{\phi}} = 9.76$ min solutions generally had larger RMS residuals than cases with $P_{\bar{\phi}} = 4.88$ min.

The best-fitting solutions for all cases with $P_{\bar{\phi}} = 4.88$ min were obtained for SAMs with $P_{\psi} = 16.21$ min with RMS values at least 10% lower than all other cases. These solutions fit the observations more naturally than the best solutions of any other candidate period pair. From an energy dissipation standpoint, this pair is also the most likely. It is the only pair tested that puts the satellite near uniform rotation, with a period ratio of 3.33 which is very close to the uniform limit of 3.229. All others are near or past the separatrix into LAM. As before, Nelder-Mead simplex optimization was used to improve on the best solutions. Fig. 32 shows the lowest RMS solution along with Part A of the light curve. The majority of the broad peaks align well in time and amplitude. Nevertheless, the solution is missing the glints present in the observations. These glints are likely generated by primary and secondary reflections off the solar array and trim tab at very specific orientations. Many simulated light curves for this period pair with slightly poorer overall fits showed a number of these glints. With a more comprehensive search algorithm and better estimate of the satellite's principal axes (current uncertainty of $\pm 5^\circ$), an even better complete solution for these SAM periods could likely be identified.

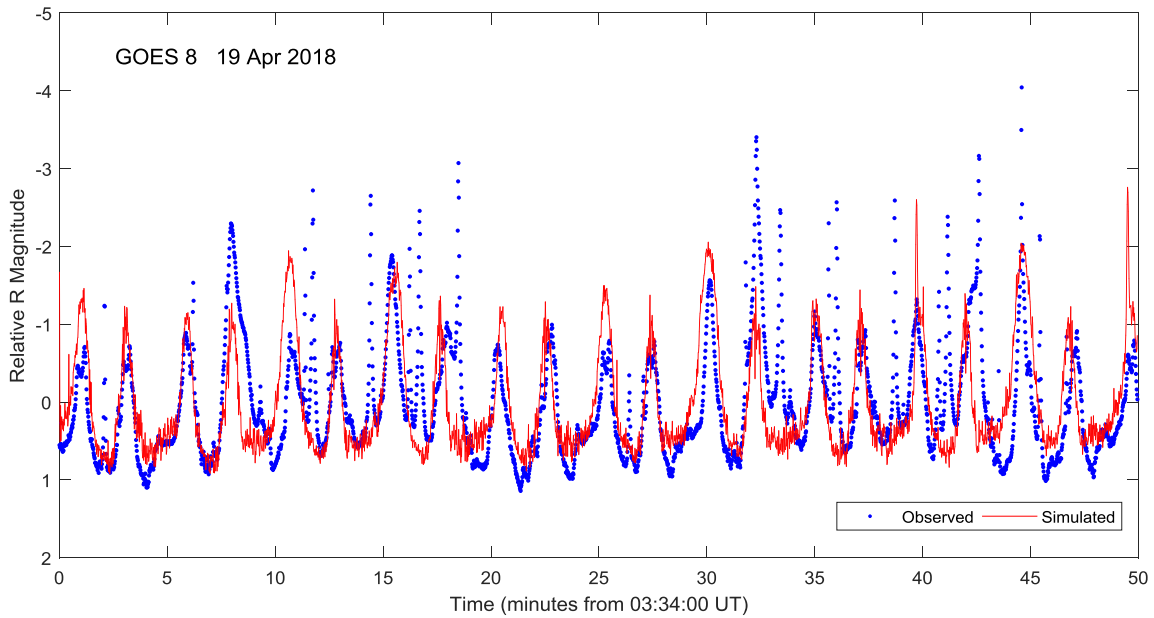


Fig. 32. Observed and Best-Fit Simulated 19 April 2018 Part A Light Curves (SAM with $P_{\bar{\phi}} = 4.876$ min, $P_{\psi} = 16.209$ min, Pole J2000 RA = 209° latitude = -27°)

8. DISCUSSION

Following the well documented deceleration from February - July 2014 [2,3], the USNO COTS observations trace out a path in which GOES 8's spin period continued to increase until early September 2014, reaching a maximum of at least 40 min. This evolution is illustrated in Fig. 33 showing a nearly linear decrease in spin rate.

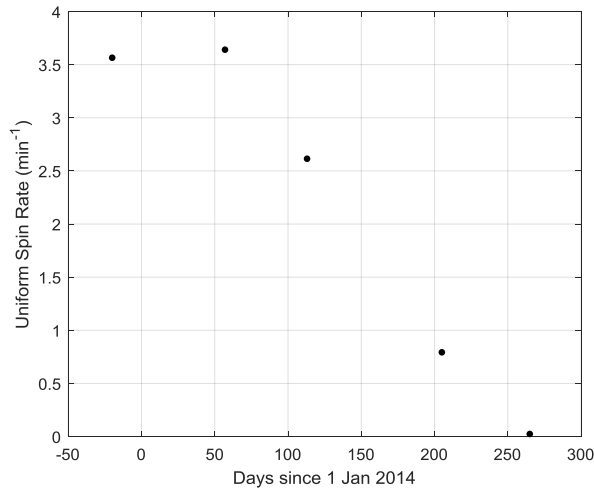


Fig. 33. GOES 8 Uniform Spin Down

Fig. 34 shows the subsequent plausible long axis precession periods from above plotted in red alongside additional USNO COTS observations (in blue) that were collected and reduced the same way as the September 2014 data in Fig. 2. For each night's observing arc, the top 10 minimum dispersion phase folded periods are plotted with data point size inversely related to phase folded dispersion (i.e. the better the fit, the larger the data point). The simulated light curve surveys demonstrated that these frequencies most likely correspond to multiples of $P_{\bar{\phi}}$ or quasi-periods, providing an informative measure of satellite's spin rate evolution. The September 2014 arcs, including those in Fig.

2, fold best on successively shorter periods from 44 – 38 min indicating that by mid-September the satellite had passed through its minimum spin rate and was spinning back up. The early 2015 COTS data show further spin up with a clear downward trend in minimum dispersion periods. The candidate precession periods obtained above are consistent with continued spin up from 12 September 2015 through at least 14 July 2016. The 2017 COTS data show a reversal of this spin up trend and point towards a second phase of very slow rotation by late 2017. Finally, the 19 April 2018 observations strongly indicate complex rotation with a precession period of 4.88 min, suggesting significant spin up in early 2018. An important trend is that the majority of observations after September 2014 exhibit more aperiodicity than can be attributed to time-varying geometry alone. This indicates the satellite spun up about its long axis in late 2014 and likely remained in at least mildly complex rotation throughout this time span. The proposed evolution over this three year span outlines at least one complete spin cycle and suggests the satellite is currently spinning up again.

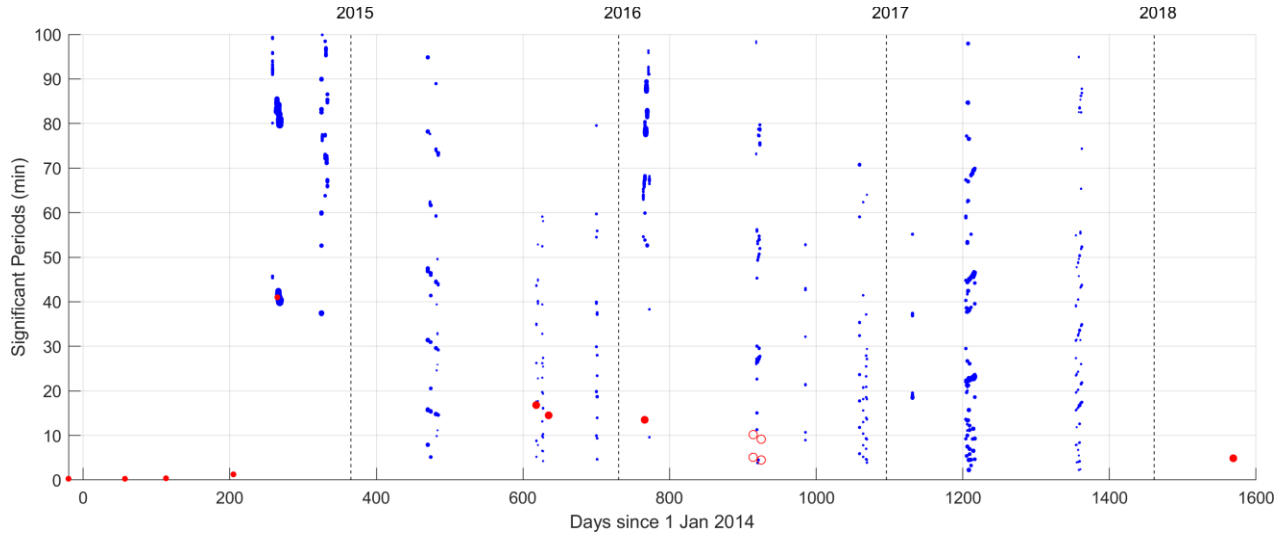


Fig. 34. GOES 8 Significant Period Evolution (candidate/known P_{ϕ} 's in red, COTS min. dispersion periods in blue)

9. CONCLUSIONS

The high fidelity simulated light curve surveys and observed quasi-periodicity demonstrate that GOES 8's tumbling light curves have clear structure dictated by its two torque-free tumbling periods and reflective characteristics. Furthermore, this ideal structure is mostly preserved with time-varying GEO observing geometry. Considering GOES 8's dynamical evolution, the observed tumbling light curves are consistent with Albuja et al.'s hypothesis that the YORP effect creates spin rate cycles and can drive satellites from uniform to complex rotation. The majority of 2015 -2018 GOES 8 light curves indicate at least mildly complex rotation, suggesting the satellite's off-axis spin rate has not completely damped out following the late 2014 spin up. Nevertheless, it is unclear how these spin rates evolved given the difficulty of identifying the long axis rotation period for slow rotation. It is likely that the largest changes in off-axis spin rates occur shortly after tumbling transitions. Further observations, particularly those taken during such transitions, and an improved light curve search/optimization approach would enhance our understanding of this off-axis spin rate evolution. More importantly, long-term dynamical simulations incorporating YORP and internal energy dissipation are needed to further explore the complex interaction between these processes.

10. ACKNOWLEDGEMENTS

The primary author would like to thank Steve Queen of NASA Goddard Space Flight Center for his assistance in developing the light curve simulator. He would also like to thank Nick Moskovitz of Lowell Observatory and Dave Monet from the Naval Observatory Flagstaff Station for helping collect and reduce GOES 8 observations presented in this paper. In addition, he would like to thank NOAA's John Tsui for providing end of life mass properties and geometry for GOES 8. Finally, this work was supported by a NASA Space Technology Research Fellowship.

11. APPENDIX

For LAMs in the long axis convention as shown in Fig. 10, P_ψ is given by,

$$P_\psi = \frac{4}{\omega_e} \sqrt{\frac{I_l I_i I_s}{I_d (I_i - I_l) (I_s - I_d)}} K(k)$$

where $K(k)$ is the complete elliptic integral of the first kind,

$$K(k) = \int_0^{\pi/2} \frac{du}{\sqrt{1 - k^2 \sin^2 u}}$$

and for LAMs,

$$k^2 = \frac{(I_s - I_l)(I_d - I_l)}{(I_i - I_l)(I_s - I_d)}$$

The expression for $P_{\bar{\phi}}$ is more complicated where $P_{\bar{\phi}} = 2\pi \frac{d\bar{\phi}}{dt}^{-1}$ and,

$$\frac{d\bar{\phi}}{dt} = \frac{I_d \omega_e}{I_l} \left[1 - \frac{(I_s - I_l) \Pi(K(k), n)}{I_s K(k)} \right]$$

where $\Pi(K(k), n)$ is the elliptic integral of the third kind,

$$\Pi(K(k), n) = \int_0^{K(k)} \frac{1}{1 + n \operatorname{sn}^2 \tau} d\tau$$

and for LAMs,

$$n = \frac{I_l (I_s - I_i)}{I_s (I_i - I_l)}$$

Here, sn is the Jacobi elliptic sine function which is periodic on $4K(k)$. The parameters $K(k)$, $\Pi(K(k), n)$, and sn can be accurately calculated with numerical routines [12].

For SAMs, the structure is very similar with P_ψ instead given by,

$$P_\psi = \frac{4}{\omega_e} \sqrt{\frac{I_l I_i I_s}{I_d (I_s - I_i) (I_d - I_l)}} K(k)$$

and for SAMs,

$$k^2 = \frac{(I_i - I_l)(I_s - I_d)}{(I_s - I_i)(I_d - I_l)}$$

The equations for $P_{\bar{\phi}}$ remain the same except that for SAMs,

$$n = \frac{I_l (I_s - I_d)}{I_s (I_d - I_l)}$$

12. REFERENCES

1. Papushev, P., Karavaev, Y., Mishina, M., Investigations of the evolution of optical characteristics and dynamics of proper rotation of uncontrolled geostationary artificial satellites, *Advances in Space Research*, Vol. 43(9), 1416–1422, 2009.
2. Cognion, R. L., Rotation rates of inactive satellites near geosynchronous earth orbit, *Proceedings of AMOS 2014*.
3. Ryan, W. H., Ryan, E. V., Photometric Studies of Rapidly Spinning Decommissioned GEO Satellites, *Proceedings of AMOS 2015*.
4. Albuja A. A., Scheeres, D. J., Cognion, R. L., Ryan, W., Ryan, E. V., The YORP effect on the GOES 8 and GOES 10 satellites: A case study, *Advances in Space Research*, Vol. 61, pp. 122-144, 2018.
5. Rubincam, D., Radiative spin-up and spin-down of small asteroids, *Icarus*, Vol. 148, pp. 2-11, 2000.
6. Lowry, S., et al., Direct detection of the asteroidal YORP effect, *Science*, Vol. 316, pp. 272-274, 2007.
7. *GOES I-M Databook*, Rev. 1, Aug. 31, 1996, <https://goes.gsfc.nasa.gov/text/goes.databook.html>, retrieved Sept. 9, 2017.
8. Pravec, P., et al., Tumbling Asteroids, *Icarus*, Vol. 173(1), 108-131, 2005.
9. Scheeres, D. J., *Orbital Motion in Strongly Perturbed Environments*, Springer, 1st edition, 2012.
10. Samarasinha, N.L., A'Hearn, M.F., Observational and Dynamical Constraints on the Rotation of Comet P/Halley, *Icarus*, Vol. 93(2), 194-225, 1991.
11. Kaasalainen, M., Interpretation of lightcurves of precessing asteroids. *Astronomy & Astrophysics*, 376, pp. 302-309, 2001.
12. Press, W. H., Teukolsky, S. A., Vetterling, W. T., and Flannery, B. P., *Numerical Recipes*, Cambridge University Press, Cambridge, UK, 3rd edition, 2007.
13. Dutre, P., Bala, K., Bekaert, P., *Advanced Global Illumination*, A K Peters/CRC Press, 2nd ed., 2006.
14. Ashikhmin, M., Shirley, P., An Anisotropic Phong BRDF Model, August 13, 2000.